Syn-convergence flow inside and at the margin of orogenic plateaus: Lithospheric-scale experimental approach

Flora Bajolet, Dominique Chardon, Joseph Martinod, Denis Gapais, Jean-Jacques Kermarrec

Syn-convergence flow inside and at the margin of orogenic plateaus: Lithospheric-scale experimental approach

Flora Bajolet[1,2,3,4] *, Dominique Chardon[1,2,3], Joseph Martinod[1,2,3,5], Denis Gapais[6], and Jean-Jacques Kermarrec[6]

1. Université de Toulouse, UPS (OMP), GET, 14 avenue Edouard Belin, 31400 Toulouse, France

2. CNRS, GET, 31400 Toulouse, France

3. IRD, GET, 31400 Toulouse, France

4. *Now at:* Université Montpellier 2, Géosciences Montpellier, Place E. Bataillon, 34095 Montpellier cedex 5, France

5. *Now at:* Université de Savoie, ISTerre, 73376 Le Bourget du Lac cedex, France

6. Géosciences-Rennes, UMR CNRS 6118, Université de Rennes 1, 35042 Rennes Cedex, France

Submitted to ***JGR – Solid Earth***

April 2015, revised August 2015

* Corresponding author, Email: flora.bajolet@gm.univ-montp2.fr

Abstract. This study investigates three-dimensional flow modes of orogenic plateaus by means of physical modeling. Experiments consist of shortening two contiguous lithospheres of contrasting strength, one being a weak plateau-type lithosphere, and the other a strong craton-type lithosphere. The lateral boundaries are either totally confined or allow escape toward a lateral foreland on one side. Two syn-convergence flow regimes are distinguished, which are governed by the balance between the gravity potential and the strength of the plateau crust and the resistance of its lateral foreland. The first regime implies transversal (orogen-normal) injection of plateau lower crust into the collision zone as a result of confinement of the plateau by an increasingly stiffer lateral boundary. As a precursor mechanism to channel flow, transversal injection responds to downward thickening of the plateau crust that is forcedly extruded into the orogenic wedge. The second regime is that of collapse-driven lateral escape of the plateau. This regime is established after a threshold is attained in the inter-plate coupling in the collision zone, which allows the gravity potential of the plateau to overcome the resistance of its lateral boundary. Under the collapse-driven escape regime (orogen-parallel), such as that governing Tibet during the last 13 Ma, most of the convergence in the plateau and the top and rear of the collisional wedge is transformed into lateral flow and extension.

Keywords: crustal flow, analog modeling, lateral escape, extrusion tectonics, orogenic plateau, hot orogen.

1. Introduction

Having attained a plateau stage, orogens are hot, owing to their high content in heat-producing elements due to crustal thickening [*England and Thompson*, 1984] and/or

because their mantle lithosphere has been thinned by thermal erosion or removed by delamination [*England and Houseman*, 1989; *Molnar et al.*, 1993; *Sandiford and Powell*, 1991; Figure 1]. Orogenic plateaus are thus particularly weak due to a reduced temperature-dependent viscosity of the crust and/or to regional partial melting [*Vanderhaeghe and Teyssier*, 2001]. As weak lithospheric regions submitted to convergence such as long-lived accretionary orogens, cordilleras and wide mature collision zones, orogenic plateaus deform dominantly by flow, which tends to maintain a low-relief surface and Moho by responding coevally to body forces due to the topography and surface forces due to convergence [e.g., *England and Houseman*, 1989; *Bird,* 1991; *Chardon et al.*, 2009].

Lateral flow in orogenic plateaus combines orogen normal shortening, forced tectonic extrusion (driven by forces applied at boundaries) and collapse-driven escape (gravitational flow) in a context of partial or full mechanical coupling between the upper mantle and the upper crust [*Royden*, 1996; *Holt*, 2000; *Tikoff et al.*, 2004; *Andronicos et al.*, 2007; *Chardon et al.*, 2011]. Concomitantly, orogen-normal extrusion of plateau lower crust into the adjoining collision wedge is inferred to occur along a channel bounded by a thrust at its base and a detachment at its top [i.e., the channel flow hypothesis; *Grujic et al.*, 1996; *Beaumont et al.*, 2001]. One must therefore consider the fundamentally three-dimensional aspects of both lateral flow inside the plateau and its potential interplay with transverse flow at the edge of the plateau. Investigating three-dimensional deformation of hot orogens is permitted in physical experiments where a thin/hot model lithosphere is shortened between two quasi-rigid walls [vice models; *Cruden et al.*, 2006; *Cagnard et al.*, 2006a; *Riller et al., 2012*]. Similar experiments have been performed with a cold/thick lithosphere [*Davy and Cobbold*, 1988]. Nonetheless, a limitation of vice models is that they simulate the shortening of a single

type of lithosphere and do not reproduce collision of a plateau with a colder, deformable lithosphere that would produce an orogenic wedge at the plateau edge. To test three-dimensional deformation modes of an orogenic plateau, the introduction of such rheological contrasts should be convenient to simulate mechanical coupling in the collision zone, which is critical to understand strain partitioning between the plateau and its foreland [*Dewey*, 1988] and potential transverse mass transfers across the plateau edge [*Beaumont et al.*, 2004]. *Ratschabacher et al.* [1991a] modeled lateral flow in experiments where a strong foreland and a non-deformable indenter flank a weak lithosphere, with variable degree of lateral confinement. However, the foreland remains undeformed in almost all experiments and the study focuses on lateral escape.

The present study investigates syn-convergence deformation and flow modes operating inside and at the margin of orogenic plateaus or hot orogens using lithosphere scaled-analog models. The experiments involve shortening of two contiguous lithospheres of contrasted strengths, a weak one and thin plateau-type lithosphere, and a strong, thick and yet deformable craton-type lithosphere. Our experimental setup is designed to investigate internal deformation of a weak plateau lithosphere being shortened under various degrees of lateral confinement. It also permits deformation of the plateau to interact with the stiff lithosphere in the collision zone by simulating various degrees of coupling between the two lithospheres.

We focus on the three-dimensional aspects of mass transfers within and at the collisional margin of the model orogenic plateau. We show that the evolving strength of the lateral foreland of the plateau primarily governs the relative magnitude of transversal (orogen-normal) and longitudinal orogenic flow. We also describe a potential precursor mechanism to channel flow that consists of forced transversal

101 extrusion of the plateau lower crust as a consequence of downward directed tectonic
102 thickening of the plateau upper crust.
103
104 **2. Experimental setup and scaling**
105 *2. 1. Model design and experimental procedure*
106 The model lithospheres float on sodium polytungstate mixed with glycol water,
107 which is a dense, Newtonian low-viscosity material modeling the asthenosphere (Figure
108 2). Ductile lithospheric layers are modeled with silicone putties (GSIR gums from
109 Rhone-Poulenc, France) that are Newtonian fluids at experimental strain rates
110 [*Weijermars and Schmeling*, 1986]. Dry Fontainebleau sand mixed with ethyl-cellulose
111 powder is used to simulate the brittle upper crust [*Davy and Cobbold*, 1991; Table 2].
112 The strong cold cratonic lithosphere consists of a brittle upper crust, a ductile lower
113 crust and a thick and dense high-viscosity lithospheric mantle (Figure 2a). The latter
114 simulates the upper part of the lithospheric mantle, which concentrates most of the
115 strength. The weak hot plateau lithosphere is modeled as a three-layer crust (i.e., a
116 lithosphere lacking its mantle part). The model consists of a brittle upper crust, a ductile
117 mid-crust and a low-viscosity lower crust simulating partial melting-induced weakening
118 (Figure 2a). The model is placed in a Plexiglas box equipped with a moving-wall
119 coupled with a piston and a motor to control shortening. Velocity discontinuities made
120 of Plexiglas plates placed on each lateral wall of the box help to localize deformation
121 away from the moving-wall and to limit boundary effects (Figure 2). Eleven
122 experiments were performed in laterally confined conditions (Figure 2a, Table 1). Three
123 experiments were performed at a medium to low lateral confinement, allowing lateral
124 escape of the model during convergence (Figure 2b). In that case, the same type of
125 model as that of laterally confined experiments was placed in a larger box, adjacent to a

126 confining silicone capable of absorbing the escape of the shortened lithospheres (Figure
127 2b). All experiments were performed at constant room temperature. There is no thermal
128 evolution of the system, density contrasts between the layers remain constant, and we
129 neglect the role of thermal diffusion and phase changes.
130 During each experiment, photographs were taken in order to map successive stages
131 of surface deformation (e.g., Figure 3). At the end of the experiment, the model is
132 freezed for at least 12 hours. There is no significant post-experiment deformation
133 because: (1) shortening is no longer active, (2) the viscosity of the silicone decreases
134 rapidly with decreasing temperature and the sudden drop in temperature prevents it
135 from flowing, (3) comparison between the last top view photo and the frozen cross-
136 sections shows similar faults locations. Then the lithospheric part of the model is
137 detached from the sodium polytungstate, buried in sand and wetted. The protective
138 sand-shell is also frozen, the block formed by the model lithosphere and the sand is then
139 cut with a circular saw to obtain serial cross-sections. For practical reasons related to
140 model preparation, the two lithospheres share the ductile crustal layer of intermediate
141 viscosity (DC; Figure 2). In the cratonic lithosphere, this layer models the whole lower
142 crust, whereas in the weak lithosphere it simulates the middle crust. Model setting
143 implies that the weak lithosphere is initially weaker than the craton and bears a 50 km-
144 thick crust at the onset of shortening. Such a setting is convenient to model an advanced
145 stage in collision and crustal thickening, which is for instance consistent with the
146 Neogene configuration of the Tibet-Himalaya system [e.g., *Replumaz et al.*, 2010c].
147
148 *2. 2. Scaling, limitations of the models and tested parameters*
149 In order to perform experiments comparable with nature, geometric and dynamic
150 similarities must be respected [*Davy and Cobbold*, 1991]. This is verified if the relation

$\sigma^* = \rho^* g^* L^*$ (1)

is respected [*Brun*, 2002], where σ^*, ρ^*, g^*, L^*, are the ratio between model and nature for stress, density, gravity and lengths, respectively. All experiments were performed under natural gravity, thus $g^* = 1$. The scaling factor for length is $L^* = 5 \times 10^{-7}$, i.e. 1 cm in experiments is 20 km in nature. In the brittle layers, the differential stress obeys the Coulomb criterion. In the ductile layers, the shear stress is

$\tau = \eta \, d\varepsilon/dt$ (2)

where τ is the shear stress, η the shear viscosity, and $d\varepsilon/dt$ the shear strain rate. The shear strain rate $d\varepsilon/dt$ depends strain localization (faulted or undeformed regions) and evolves through time. A good approximation of the bulk shear strain rate (for the entire model and whole duration of the experiment) is

$d\varepsilon/dt \sim V/L$ (3)

where V is the imposed shortening rate and L the length of the shortened area. Equation (2) is then equivalent to

$\tau \sim \eta V/L$ (4)

In all experiments, the brittle layer is modeled using a mix of dry sand and ethyl-cellulose powder whose cohesion is negligible. According to *Schellart* [2000] and *Lohrman et al.* [2003], the friction coefficient of sprinkled sand varies between 0.5 and 1.2 for sifted sand and for the range of normal stresses considered in our experiments. In order to estimate the friction coefficient of the sand we evaluated the dip of reverse and normal faults in simple experiments, and we concluded that the friction angle is ~ 30° for the sprinkled sand we used, i.e. the friction coefficient is close to 0.6. The viscosity of the silicone layer that models the ductile lithosphere varies between 9.5×10^3 Pa s and 3.81×10^4 Pa s (Table 2). Figure 2 shows the strength profiles of the weak and cratonic lithospheres for the reference experiment, strength values being summarized in

176 Table 3. The overall model strength profiles for the lithospheres respect the scaling law
177 (Figure 2) and makes our experiments comparable with nature. However, the ratio
178 between the viscosity of lithospheric layers and that of the asthenosphere is ~ 3 x 10^4,
179 which is more than one order of magnitude larger than in nature [*Loiselet et al.*, 2009;
180 *Schellart*, 2010]. In our experiments, the asthenosphere essentially exerts normal
181 hydrostatic stresses on the lithosphere. This should not affect fundamentally the
182 evolution of our experiments, since neither a subduction zone nor any large deformation
183 appear at the lithosphere/asthenosphere boundary in the models. In our experiments,
184 lithospheric deformations only result from the applied boundary conditions and from
185 the collapse of lithospheric plates, not from asthenospheric fluxes.
186 Model lithospheres respect the scaled ratio of crust density over lithospheric mantle
187 density (Table 2). For practical reasons, the density of the asthenosphere in the models
188 is higher than that of the lithospheric mantle (1.75 and 1.56 respectively) whilst they are
189 of the same order in nature. This has an impact on the gravity potential of the
190 lithospheres that is overestimated. We calculated Argand numbers (Ar) characterizing
191 the ratio of body forces over tectonic forces, to check if body forces alone are large
192 enough to result in lateral escape (Appendix A, Table 4).
193 $Ar = F_B/F_T$ (5)
194 If Ar>1, the lithosphere is unstable and can potentially collapse; whereas for Ar<1 the
195 body forces may be supported by the strength of the lithosphere. This number is
196 increased by a factor ~2 when the density of the liquid modeling the asthenosphere rises
197 from 1.56 to 1.75. Hence, lateral escape is favored in our experiments if permitted by
198 lateral boundary conditions (unconstrained experiments). In nature, many other
199 phenomena that are not reproduced in experiments may also favor lateral escape, as for
200 instance, the subduction of an oceanic plate of the lateral foreland that would modify the

lateral traction exerted on the collision zone, as in SE Asia for the Tibetan plateau. Our unconfined experiments reproduce the deformation of a continental collision zone in which the lateral tectonic boundary conditions favor lateral escape. On the other hand, confined experiments show the evolution of a craton/plateau collision zone in which lateral boundary conditions oppose it. Another limitation of our models is that they do not reproduce the early stages of oceanic and continental subduction, which implies that we neither take into account the influence of inherited structures from these stages, nor simulate processes such as pre-collisional subduction, back arc extension, or slab-break-off. We choose analog materials that reproduce a mature plateau (weak and thick crust), corresponding to the collisional stage. Although no oceanic subduction occurs, the continental cratonic lithosphere underthrusts the plateau along a large-scale shear zone and reproduces a realistic collision dynamics at the suture (see below).

The impact of several parameters has been tested: (1) the shortening velocity, which sets the strength of the ductile layers and the degree of brittle-ductile lithospheric coupling, (2) the thickness and viscosity of the crustal ductile layers to test different strength contrasts amongst crustal layers and between the plateau and cratonic lithospheres, and (3) the thickness of the silicone layer that opposes lateral escape (Table 2).

3. Results

Performing an experiment with the same experimental settings twice and stopping them at two different amounts of shortening allowed us to reconstitute successive deformation stages in cross-section view. Comparison of the serial cross-sections of a same model also helps constraining the sequential development of the structures given the lateral gradient of finite shortening existing between the sides of the box (near the

velocity discontinuity generated by the tip of the lateral wall of the piston) and its center (Figures 2 and 3). In all the figures, the weak lithosphere is placed on the left hand side of the maps and cross-sections. In the text, pro-thrusts designate thrusts verging towards the cratonic foreland (the pro-side of the orogen), whilst retro-thrusts designate thrusts verging towards the hinterland (the retro-side of the orogen).

3. 1. Laterally confined experiments

3. 1. 1. Structures and kinematic evolution

There is a remarkable consistency in the development mode of the structures and flow patterns in all the laterally confined experiments. Upper crustal shortening first affects the weak lithosphere, which absorbs ca. 70% of the total shortening. From 3-4% of shortening, a first series of retro-thrusts forms in the weak lithosphere, each fault evolving into a conjugate couple of reverse faults delimiting pop-downs [e.g., Figure 4c and 4d; see *Cagnard et al.*, 2006b]. Each conjugate fault set is abandoned when a new pop-down forms. In experiments with contrasted brittle crust thicknesses between the two types of lithospheres (Figures 4b to 4d, 4f and 5), the last conjugate fault set forms at the lithosphere boundary at 10-15% shortening. It remains active until the end of the experiment. The retro-thrust of this late conjugate couple is predominant.

Shortening of the cratonic crust is localized along a limited number of thrusts delimiting pop-ups, which become generally inclined or overturned cratonwards 3-5% of shortening after they form (e.g., Figures 3, 4a, 5). Ductile layers are generally thickened, especially the low-viscosity lower crust in the weak lithosphere, whose thickness is doubled after 30% of shortening (Figures 3 and 4). The mid-crust of the plateau is thickened as much as its weak lower crust; whereas the ductile cratonic crust undergoes less thickening (25% after 30% of bulk shortening).

The plateau lower crustal layer is thrust upon the cratonic lithospheric mantle, initiating continental scale underthrusting of the cratonic mantle along a pro-shear zone. This lithospheric shear zone is shown in Figures 3 to 5 by white arrows. The plateau lower crustal layer keeps a flat floor and thickens as a symmetrical dome (Figure 3) that becomes overturned above the lithospheric pro-shear zone (Figures 4a to 4d). Asymmetrical doming results in a wedge shape of the plateau lower crust, whose roof makes the back limb of the dome and dips toward the hinterland. As the dome amplifies, it is obliquely injected into the cratonic lower crust, which is in turn underthrust beneath the inverted limb of the dome (Figures 4a to 4d). A far-field channel flow effect is produced in the cratonic lower crust by injection of plateau lower crust into the foreland (e.g., Figure 4e).

The back-limb of the dome shows upright mullions or folds interpreted as a consequence of distributed shortening (Figures 4a to 4d). This attests to limited crustal-layering parallel shearing at the roof of the weak lower crust and to dominant homogeneous thickening of the plateau at the rear of the dome. This also means that part of the mid crust of the weak lithosphere is transported cratonward on the roof of the weak lowermost crust. The top of the dome, once amplified, is taken into a flat retro-shear affecting the upper mid-crust, which is marked by backward deflection of former mullions or folds at the dome's crest (Figures 4b, 4d, 5). This shear zone emerges as the last active retro-thrust making the boundary of the plateau crust (Figures 4b, 4d, 5). The boundary between the two types of brittle crusts migrates twice as much more towards the hinterland than the intersection between the underthrusting shear plane and the asthenosphere. This explains the large magnitude of mid- and upper crustal back shearing above the overflowing lower crust of the weak lithosphere. In the cratonic lithosphere, the last pro-thrust propagates upward from the underthrusting shear zone

276 (e.g., Figures 4d and 5). Importantly, no net unroofing of the plateau weak lower crust
277 occurs as a consequence of doming and lower crust overflow. Indeed, the crest of the
278 dome does not attain shallower depths than the initial depth of the top of the plateau
279 weak lower crustal layer.
280
281 3. 1. 2. Sensitivity to parameters
282 The shortening velocity, by controlling the degree of coupling between the
283 lithospheric layers, affects the style of deformation. For a high velocity, thrusts remain
284 active for a shorter time period and are abandoned more quickly. An increase in
285 coupling (higher velocity) is also expressed by earlier faulting in the cratonic crust, and
286 a greater dip and lower finite displacement of the lithospheric shear zone (45° for 4 cm
287 h^{-1} in Figure 4c against 20° for 0.4 cm h^{-1} in Figure 4d). An increased strength (i.e.
288 velocity) also leads to less backward displacement of the suture. Therefore, for a high
289 degree of coupling, shortening is preferentially accommodated by thickening instead of
290 by underthrusting and/or injection.
291 Using the same thickness of the brittle crust over the entire model favors pro-thrusts
292 and pop-downs between 20 and 30% of shortening (Figures 3 and 4a). Finally, changing
293 the thickness and rheology of the plateau crust to highly over-thickened and less viscous
294 (Figures 4e and 4f) favors distributed deformation and limited stacking of pop-downs in
295 the plateau. In this situation, instead of dipping towards the hinterland, the roof of the
296 plateau lower crust is either flat or cratonward dipping, which suggests an active role of
297 the gravitational potential of the thickened crust on the dynamics of cratonward
298 extrusion.
299
300 *3. 2. Experiments with lateral escape*

301 3. 2. 1. Structures and kinematic evolution in map view

302 In this section, we will first describe experiment F2 (Figure 6), taken as a reference
303 experiment. We will then evaluate the effect of an increased shortening velocity
304 (experiment F3, Figure 7) and of an increased strength of the silicone layer opposed to
305 lateral escape (experiment F1, Figure 8). The term external refers herewith to the part of
306 the model located close to the boundary where lateral escape is permitted; whereas the
307 term internal, which refers to the confined boundary side of the model.

308 From the beginning of the experiment, the entire model escapes laterally, forming an
309 outwardly convex arch. Deformation nucleates as conjugate strike-slip fault sets
310 affecting both lithospheres (Figure 6). The main intersection between these faults
311 defines a sag basin marking the transition between an internal domain dominated by
312 reverse faulting and transpression, and an external domain dominated by extension and
313 transtension (Figure 6). As shortening increases (16%), the plateau lithosphere
314 concentrates the deformation by developing an anastomosing network of longitudinal
315 transpressive faults (pro and retro) that propagate towards the external domain in the
316 form of conjugate strike-slip faults (Figure 6). Between 7.5 and 21 % shortening, a
317 retro-thrust nucleates and propagates at the boundary of the two lithospheres. The
318 hinterland-side fault system of the plateau is abandoned and the rest of the plateau fault
319 network is shortened and laterally elongated as a result of fault rotations. A new dextral-
320 oblique thrust propagates obliquely across the cratonic lithosphere by joining the piston
321 and the plateau. This fault defines the front of the external triangle-shaped half of the
322 cratonic lithosphere that is deformed. Continuous widening and clockwise rotation of
323 the grabens attest to combined lateral stretching and dextral shearing of that triangle
324 which responds to faster lateral stretching and escape of the plateau lithosphere
325 compared to the cratonic lithosphere. Overall shortening induces partitioning of the

326 deformation between the two lithospheres. The cratonic lithosphere undergoes limited
327 shortening and heterogeneous lateral extension. The weak lithosphere deforms by bulk
328 homogeneous pure shear deformation, which is accommodated by an anastomosing
329 network of transpressive faults [*Cagnard et al.*, 2006a; *Cruden et al.*, 2006; *Riller et al.*,
330 2012]. To summarize, transverse shortening and lateral escape of the plateau by bulk
331 pure shear induce a combination of heterogeneous simple shear and pure shear in the
332 cratonic lithosphere (Figure 9).

333 Increasing the strength of the ductile layers by increasing the velocity of shortening
334 leads to a lesser amount of lateral escape (experiment F3; Figure 7), especially if
335 compared to the amount of shortening (Figure 10d). The smaller thickening/escape ratio
336 in this experiment results from the weaker influence of body forces due to density
337 contrasts compared to forces arising from convergence velocity. The plateau lithosphere
338 undergoes more escape than the cratonic lithosphere. The retro-thrust at the lithospheric
339 boundary does not propagate beyond the central sag basin (Figure 7). Deformation
340 concentrates along the hinterland side of the plateau and over its entire length by
341 activation of successive straight thrusts (Figure 7). On both sides of the sag basin, two
342 large areas of the plateau remain nearly undeformed against the hinterland deformation
343 belt (Figure 7). Though not visible, deformation occurs at the lithospheric contact in the
344 external part of the model since diffuse shear is required along this boundary in order to
345 explain higher differential escape of the plateau. To summarize, an increased strength of
346 the ductile layers caused by a higher shortening velocity induces (1) smaller amount of
347 lateral escape compared to the amount of shortening, (2) differential escape of the
348 plateau and therefore partial decoupling between the two lithospheres, (3) strain
349 partitioning inside the plateau, and (4) limited deformation of the cratonic lithosphere
350 (Figure 9).

For a strength and thickness of the lateral silicone three times that of experiments F2 and F3, the cratonic lithosphere remains virtually undeformed until late stages of shortening, and the plateau is indented and partly escaped (experiment F1; Figure 8). Bulk pure shear strain of the plateau lithosphere is achieved by an anastomosing network of transpressive faults due to the densification and rotation of an early strike-slip conjugate fault network. Spreading in the escaped plateau peninsula is accommodated by normal faults having a strike-slip component (Figure 8). To summarize, an increase in strength at the lateral boundary favors decoupling between the two lithospheres, pure shear assisted escape of the plateau, and spreading confined to the escaped part of the weak lithosphere (Figure 9).

3. 2. 2. Structures and kinematic evolution in cross-section

As a significant part of the convergence is absorbed by lateral escape at the earliest stages of shortening, cross-sections of the free boundary experiments provide insights into the earliest stages of convergent deformation. In the inner part of the model, the earliest increments of shortening are accommodated by indentation of the plateau lower crust by the cratonic lithospheric mantle (Figures 6 and 7). The future overflowing dome of plateau lower crust initiates as a result of this indentation, which is also accompanied by doming of the cratonic mantle (Figures 6 and 7). The retro-thrust marking the lithosphere boundary in the upper crust may possibly be related to the early indentation process (Figures 6 and 7). In the external part of the model, the two domes involved in the indentation process either never appeared, or collapsed. The net throw of the retro-thrust is greater than in the internal part of the model (Figures 6 and 7). This is interpreted as a consequence of escape-enhanced lateral thinning of the plateau lithosphere (see below).

376

377 3. 2. 3. Three-dimensional analysis

378 We performed a three-dimensional finite strain analyses (Appendix B) to
379 quantify the deformation along the principal axis of the strain ellipsoid λ_1 (maximum
380 elongation), λ_2 (intermediate) and λ_3 (maximum shortening). It shows that λ_1 is
381 horizontal and orogen-parallel and λ_3 is horizontal and orogen-normal in the plateau
382 lithosphere in all experiments with lateral escape (Figure 9). A general transition is
383 documented from vertical flattening in the internal part of the plateau to horizontal
384 plane strain or constriction in the external part of the plateau (Figure 9). For strong
385 coupling between the two lithospheres (experiment F2; Figures 6 and 9), flow toward
386 the lateral boundary compensates thickening, and the external domain of the plateau is
387 deformed by horizontal plane strain. For partial decoupling between the two
388 lithospheres resulting from a higher shortening velocity (experiment F3; Figures 7 and
389 9), lateral constriction in the external part of the plateau lithosphere attests to a
390 component of thinning superimposed on orogen-normal shortening. Horizontal
391 constriction prevails in the cratonic lithosphere in response to combined lateral
392 stretching and vertical thinning [*Merle and Gapais*, 1997; *Teyssier and Tikoff*, 1999].
393 No cross-sections are available for the indentation experiment characterized by a higher
394 strength of the confining silicone (experiment F1; Figures 8 and 9c), but surface
395 deformation shows that the cratonic lithosphere remains virtually undeformed.
396 Conversely, one may expect stronger vertical flattening in the internal part of the
397 plateau lithosphere. The presence of normal faults in the escaped peninsula (Figure 8,
398 9c), attests to significant thinning due to spreading. To summarize, lateral finite thinning
399 of the weak lithosphere characterizes the three experiments.

400 Strain intensities (Appendix B) are of the same order of magnitude for F2 and F3
401 experiments, and always lower for the cratonic lithosphere (from 0.7 to 1.5) than for the
402 weak lithosphere (from 1.1 to 1.7). In the weak lithosphere, the strain intensity
403 parameter ε_s [*Nadai*, 1950] is minimum at the center of the model (Table 4), maximum
404 at the external boundary, and intermediate in the internal domain. This is interpreted as
405 the superimposition of thickening near the confined wall onto a strain gradient due to
406 the laterally increasing component of longitudinal stretching. Higher strain intensity
407 near the lateral boundary is interpreted as the result of the superimposition of a
408 gravitational component of flow onto the bulk shortening strain ellipsoid. Strain
409 intensities in the cratonic lithosphere, though very low, also increase towards the lateral
410 boundary (Table 4).
411 Lateral escape patterns for strong coupling (F2 experiment) or partial coupling (F3
412 experiment) between the two lithospheres are comparable (Figures 10b and 10c).
413 Lateral escape is fast at the beginning and decreases rapidly within 5 hours to a nearly
414 steady value (Figures 10b and 10c). In experiment F2, early escape is accommodated by
415 overall thinning of model lithospheres (total escaped area greater than the area lost by
416 the advance of the piston up to 6 hours time; Figure 10b). At the end of both
417 experiments, total lateral escape had roughly accommodated half of the area lost by the
418 advance of the piston, the remaining half of which having been absorbed by lithospheric
419 thickening (Figures 10b and 10c). In the experiment with a thicker confining silicone
420 (F1; high strength of confining silicone, complete decoupling between the two
421 lithospheres, indentation of the weak lithosphere by the craton), lateral escape evolves
422 linearly with time. The escaped surface consists exclusively of weak lithosphere and
423 remains low even at the end of the experiment (50 cm^2 vs. 150 cm^2 for experiments F2
424 and F3; Figure 10a to 10c). This analysis suggests that lateral escape is far more

425 sensitive to the resistance at the lateral boundary than to the strength of the lithospheres,
426 as observed in experiments by *Ratschbacher et al.* [1991a].

427 The evolution of the gravity potential and stability of the model lithospheres may be
428 quantified using the Argand number (Ar; eq. 4 and Appendix A). We calculated Ar of
429 the cratonic and weak lithospheres for the initial and final configurations of the
430 experiments (Table 4; Figure 9). This parameter depends on the buoyancy of the
431 lithospheric mantle that is overestimated in our models (Table 2). Consequently, Ar is
432 also overestimated (up to a factor 2), and collapse of the model resulting in lateral
433 escape is favored by the density layering we adopted. As discussed in section 2.2, other
434 processes not reproduced in our models can favor lateral spreading of the plateau. Then,
435 this choice in the parameters may simulate natural situations, for example when lateral
436 oceanic subduction zone occurs while the collision is active, as it is the case in SE Asia.

437 In all experiments, the cratonic lithosphere is also potentially unstable at the
438 beginning of the experiment (Ar>1). This is attested by the development of grabens and
439 deformation leading to lateral constriction. Nonetheless, the significant differential
440 finite strain and lateral escape undergone by the two lithospheres is enhanced by a
441 higher strength of the cratonic lithosphere compared to the weak lithosphere. Although
442 the cratonic lithosphere is potentially unstable, its resistance prevents a rapid collapse.
443 Collapse efficiency and velocity also depend on the resistance at the lateral boundary
444 and on the degree of coupling between the two lithospheres, which are not taken into
445 account in the expression of the Argand number. Furthermore, when the two
446 lithospheres are coupled (experiments F2 and F3), lateral stretching of the cratonic
447 lithosphere primarily adjusts to lateral escape of the deforming weak lithosphere (Figure
448 9). The above considerations suggest that despite the experimental limitations, the

449 dynamic analysis of deformation inside and at the collisional boundary of the weak
450 lithosphere remains valid.
451 In experiment F1 including a thick lateral confining layer (Figure 8, Table 4), the
452 initial negative Argand number of the weak lithosphere is not realistic for simulating an
453 orogenic plateau. These initial experimental conditions may rather simulate a thin hot
454 back arc domain precursor of an orogenic plateau. During experiment, the thickening of
455 the weak lithosphere increases its Argand number, which should in turn favor lateral
456 escape. Then, the weak lithosphere should not escape right away, but only after a
457 significant amount of shortening-induced thickening. However, lateral escape takes
458 place with a constant rate during the entire the experiment (Figure 10a). This apparent
459 inconsistency shows that horizontal stresses resulting from the shortening of the weak
460 lithosphere are larger than horizontal stresses arising from density contrasts with the
461 lateral confining medium. In these conditions, part of the shortening is accommodated
462 by lateral escape. Such a configuration reflects a forced tectonic extrusion mechanism
463 such as that modeled by *Tapponnier et al.* [1982] and in the strongly confined
464 experiments of *Ratschbacher et al.* [1991].
465 For strong (F2 experiment) or partial (F3 experiment) coupling between the two
466 lithospheres (case of a weaker lateral foreland), the initial Argand number of the weak
467 lithosphere is significantly higher than that of the cratonic lithosphere (Table 4). At the
468 beginning of experiments, the main driving mechanism of escape is collapse, as attested
469 by the evolution of the escape versus thickening ratio through time (Figure 10d).
470 Collapse-driven escape is fast at the early stages of the experiment. As the lateral
471 foreland thickens with time, the Argand number of the plateau drops and the escape rate
472 decreases accordingly and eventually stabilizes (Figure 10b, 10c, and 10d). At that
473 stage, the models become governed by forced tectonic extrusion in a configuration that

474 is close to that of experiment F1 with a high strength lateral foreland. In other words,
475 the evolving strength of the lateral foreland exerts a prime control on the dynamics of
476 hot orogens, particularly on their capacity to collapse laterally. Such an influence is
477 similar to that observed by *Davy and Cobbold* [1988].
478
479 **4. Discussion**
480 Models describing the dynamics of the Himalaya-Tibet orogen should be consistent
481 with geological observations, earthquakes distribution and deep structure. Several
482 models have addressed these issues. For example *Grujic* [1996] or *Beaumont et al.*
483 [2001; 2004] focused on the transverse mass transfers in the collision zone, and *Royden*
484 *et al.* [1997, 2008], *Clark and Royden* [2000] try to explain the topographic gradient and
485 lateral escape at the eastern edge of the plateau. The differences between the frontal and
486 lateral margins arise from boundary conditions (collision with strong lithosphere vs.
487 partially free boundary, respectively), deep structure (underthrusting of India or not),
488 orientation with respect to the direction of convergence (parallel vs. perpendicular) and
489 surface factors (climate, erosion rates). This results in different crustal flow modalities
490 and timing. For the south margin of the plateau, the channel flow model explains
491 exhumation of high grade rocks (High Himalayan Crystalline) bounded by a thrust at its
492 base (Main Central Thrust, MCT) and a detachment at its top (South Tibetan
493 detachment, STD) alongside with focused erosion at the surface. Cratonward injection
494 of plateau lower crust in the collision zone as observed in our 2D models provides
495 insights into the channel flow process (Figures 3 and 4). At the eastern margin of the
496 Tibetan plateau, eastward flow of weak lower crust material without exhumation could
497 explain the topographic gradient and GPS motions in the area. The lateral flow patterns
498 of our 3D models (Figures 6 to 8) allow addressing the mechanism of eastern growth /

499 escape of the Tibetan plateau. It is important to consider that despite their obvious
500 kinematic differences, both the transverse and lateral flow processes are ultimately
501 driven by gravitational collapse and/or forced tectonic extrusion of plateau lower crust
502 [*Bird*, 1991; *Royden et al.*, 1997; *Shen et al.*, 2001; *Beaumont et al.*, 2004]. In the
503 discussion, we shall first focus on strain partitioning at the surface and at depth, then on
504 the transversal flow at the India-Asia plate boundary, and finally discuss three-
505 dimensional aspects of the interplay between transversal and lateral flows. As our
506 models do not involve erosion or temperature variations, we shall not discuss surface
507 processes or metamorphism issues.
508
509 *4.1. Strain partitioning and kinematics*
510 In the Himalaya-Tibet orogen, strain is spatially partitioned, with dip-slip reverse
511 faulting at the orogenic front and transpression in the syntaxes and north of the Kunlun
512 fault, whereas the plateau undergoes transtension, and strike-slip deformation dominates
513 East of the Longmen Shan and Xianshuihe fault [*Andronicos et al.*, 2007]. Our models
514 reproduce well most of this pattern. In 2D and 3D, thrusting initiates at the lithospheres
515 boundary and at the backstop at early stages, with a strike-slip / transpressive
516 deformation component for 3D models forming anastomosed fault networks (e.g.
517 Figures 3 and 6). This confirms recent studies challenging the view of reverse thrusting
518 propagating from the suture to the North [e.g. *Tapponnier et al.*, 2001] and attesting
519 distributed deformation in the plateau with Paleocene/Eocene faulting in north Tibet
520 [e.g. *Zhang et al.*, 2004; *Clark et al.*, 2010]. The weak plateau lithosphere squeezed
521 against the strong Tarim basin / craton in the north, represented by the back wall of the
522 box in our experiments, can deform early far from the collision zone. The Himalayan
523 plate boundary is complex with transpressive deformation along the Karakorum fault,

524 the suture and the Jiali fault, which is connected with north-south striking grabens from
525 the west – central part of the plateau (Fig). Right-lateral strike-slip shearing (early to
526 mid-Miocene) and east-west extension (mid-Miocene) are very close in age and may
527 have been coeval in east and central Tibet [*Murphy et al.*, 2002, 2010; *Taylor et al.*,
528 2003; *Searle et al.*, 2011 and references therein]. Our experiments reproduce very well
529 this pattern and are consistent with previous experiments [*Ratschbacher et al.,* 1991a]
530 with the development of a large-scale transpressive fault at the boundary between craton
531 and plateau lithospheres, coeval with the opening of conjugate grabens (Figures 6 and
532 7). The grabens rotate clockwise to accommodate lateral escape but stay roughly
533 parallel to each other and do not show changes in strike from west to east as in Tibet
534 [*Kapp and Guynn*, 2004]. The plate boundary stays almost straight unlike the arcuate
535 Himalaya bounded by syntaxes. This implies that processes not reproduced in the
536 experiments and controlled by earlier oceanic subduction stages and/or the shape of
537 Greater India [*Ali and Atchinson*, 2005; *Replumaz et al.*, 2010c; *van Hinsbergen et al.*,
538 2011; *Bajolet et al.*, 2013] would be responsible specific features of the orogen such as
539 (i) the Himalayan orocline and the variable strike of rifts potentially due to oroclinal
540 bending [*Ratschbacher et al.*, 1994], (ii) the lateral variations in strain orientation along
541 the orogenic front [*Seeber and Pecher*, 1998; *Kapp and Guynn*, 2004] and (iii)
542 southward propagation of the orogenic front [*Murphy and Copeland*, 2005; *Bajolet et*
543 *al.*, 2013]. In our models, the grabens are also restricted to the plate boundary area and
544 within the cratonic lithosphere, and transpression is confined to the inner plateau
545 (Figures 6 to 8), whereas central Tibet is under transtension [*Andronicos et al.*, 2007].
546 The boundary between these domains is also more irregular in nature than in our
547 experiments [e.g. *Ratschbacher et al.*, 2011]. Possibly because in our experiments the
548 rheological contrast between the plateau and the craton localizes this boundary.

549 Moreover, the Tibetan plateau's width is variable (from ca. 400 km near the west
550 syntaxe to 1000 km in its center) whereas it is constant in our experiments. In our 3D
551 models, gravitational collapse is mainly accommodated by lower ductile flow, whilst it
552 is also partially accommodated in the upper crust in Tibet by active grabens.
553 Transtension is observed in the less deformed external part of the 3D models that rotates
554 clockwise during escape (Figures 6 to 8). Experiments F2 and F3 (Figure 6 and 7) with
555 a thin confining layer show large amount of escape as in east Tibet but limited rotation.
556 Experiment F1with a thick confining layer (Figure 8) reproduces well the overall
557 rotation and deformation pattern of extruded SE Tibet between the Red River and
558 Sagaing faults, but with a small amount of escape. This would confirm the
559 heterogeneity in lithospheric strength east of Tibet, with an overall weak lateral foreland
560 allowing eastward escape, but bearing a strong Sichuan basin resisting and redirecting
561 lateral escape to the SE [*Cook and Royden*, 2008; *Robert et al.*, 2010a].
562 If it is now well established that deformation is distributed within the Tibetan
563 plateau, strain localization at depth is still debated, especially in eastern Tibet.
564 Earthquakes distribution [*Clark and Royden*, 2000; *Steck et al.*, 2001; *Andronicos et al*.,
565 2007; *Priestley et al.*, 2007] and geophysical imaging [*Bai et al.*, 2010; *Liu et al.*, 2014;
566 *Bao et al.*, 2015] suggests that 1) the mid/lower crust is heterogenous with weak regions
567 (interconnected or not) and stronger ones, 2) some faults are rooted in the deep crust
568 and channelize crustal flow, whereas others are restricted to the upper crust. In our
569 experiments, the fact that the most external (escaped) part the models remains mostly
570 undeformed and that silicone layers are homogeneous does not allow us to model
571 complex flow patterns at depth and test the hypotheses mentioned above.
572
573 *4. 2. Transverse mass transfers at plateau edge*

574 Our experimental results help reconstruct a sequence of deformation at the contact
575 between a hot and a cold lithosphere under ongoing convergence such as the Himalaya
576 collision zone (Figure 11). Early shortening is absorbed dominantly by indentation of
577 the hot lithosphere by the mantle layer of the cold lithosphere. In the weak lithosphere,
578 ongoing convergence is accommodated by distributed thickening and by burial of upper
579 crust by the formation of pop-downs [*Cagnard et al.*, 2006b]. Pop-downs are not
580 observed in the cratonic lithosphere because strong lithospheric mantle prevents
581 downward motion of crustal material. Instead, shortening is accommodated by
582 thickening and pop-ups. Indentation at depth evolves into the subduction of the cratonic
583 mantle beneath the weak lithosphere. Decoupling along the continental subduction
584 enables overflow and later injection of the lower crust of the hot lithosphere into the
585 orogenic wedge. Shortening of the cold lithosphere induces moderate crustal thickening
586 and strain localization along foreland-verging thrusts rooted in the subduction shear
587 zone. The shear zone accommodating back-shearing at the roof of the overflowing hot
588 lower crust emerges as a retro-thrust at the suture. In other words, transverse advection
589 of weak lithosphere lower crust produces indentation of the foreland crust by coeval
590 activation of (1) retro-fold-and-thrust belt whose front coincides with the suture, and
591 (2) a pro- (subduction) shear zone rooting in the crust-mantle boundary. The surface
592 trace of the suture zone migrates towards the hinterland concomitantly with cratonward
593 injection of lower crust and continental subduction. Interestingly, these features and
594 kinematics are also produced in channel flow numerical experiments where the craton
595 lower crust does not subduct with, and is decoupled from, the underlying lithospheric
596 mantle and the trench is fixed [*Beaumont et al.*, 2004]. In numerical models with trench
597 advance as in the India-Asia collision, the motion of the suture (proward or retroward)
598 depends on the trade-off between the subduction velocity and the denudation intensity

599 at the orogenic front. Our experiments do not simulate early stages of subduction and
600 the cratonic upper crust is not forced to subduct beneath the plateau lithosphere as in
601 numerical models, which may explain the migration of the surface trace of the suture
602 toward the hinterland. However, the suture, branching on a lithospheric shear zone,
603 controls underthrusting of the cratonic lithospheric mantle at a shallow angle and a fold-
604 and-thrust belt develops at the lithospheres boundary. This configuration is similar to
605 the India-Asia collision where Indian mantle underthrusts the Tibetan lithosphere over a
606 large area [*Jimenez-Munt et al.*, 2008; *Li et al.*, 2008]. One may infer from the
607 experiments that in case of efficient erosion at the orogenic front, the dome of lower
608 plateau crust could be significantly exhumed. Such an exhumation would stop backward
609 flow at the roof of the dome and may change the kinematics at the suture. Therefore, the
610 trench-fixed dynamics reproduced in the experiments may be only transient and coeval
611 with dome amplification and ascent, before trench-advance occurs in late collisional
612 stages.

613 Keeping a nearly stationary flat Moho and topographic surface, the plateau crust
614 shortens and thickens by preferential downward motions that are transformed into
615 cratonward (i.e., transverse) extrusion of lower crust (Figure 11). The initiation and
616 amplification mode, structure and kinematics of the lower crustal dome indenting the
617 collisional wedge compare to those of hot fold nappes and may reflect early stages of a
618 channel flow process. However, in contrast with fold nappes that are fed from below by
619 upward extrusion of collisional wedge crust [*Merle and Guillier*, 1989; *Duretz et al.*,
620 2011], our model implies feeding of the transversally extruding lower crust by
621 downward burial of thickened plateau crust.

622 In channel flow models as set up by *Beaumont et al.* [2004], the shape and amplitude
623 of cratonward flow are determined by the conditions at the plate boundary and the

624 denudation intensity at the orogenic front. Exhumation of lower crust is achieved for
625 denudation rates of ca. 1cm yr^{-1} and a fixed shape of the subduction fault assuming a
626 non-deformable upper mantle. These parameters ensure the formation of a large-scale
627 channel in the mid-crust (injecting the craton over several hundreds of kilometers)
628 unlike the structure observed in our models. The fact that no net exhumation of the
629 dome takes place in our models requires either a change in the boundary conditions of
630 the injection, or an additional phenomenon not modeled here and permitting the hot
631 lower crust to reach the surface. An increase of mechanical coupling between the two
632 lithospheres will inhibit subduction and transversal flow. This should also favor the
633 nucleation of a thrust ramp below the advancing dome, which would form a fault bent
634 fold involving the dome, thereby enhancing focused erosion and ultimately exhumation
635 of the dome (Figure 11). No structure comparable to the South Tibetan Detachment
636 (STD) is formed during our experiments, most probably because the exhumation of the
637 dome is not complete. However, toppling of the backlimb of the dome on the ramp
638 would turn the retro-thrust system accompanying transversal injection into a hinterland-
639 dipping detachment system comparable to the STD (Figure 11, e.g., *Godin et al.*, 2011).
640 Whatever the mechanism controlling the kinematics of this detachment (gravitational
641 collapse or extension-assisted mountain building), the formation of a crustal ramp and
642 its consequences could set favorable conditions to establish channel flow as envisaged
643 by *Beaumont et al.* [2001, 2004]. In the scenario exposed above, back thrusts at the rear
644 of the exhumed lower crust (former dome) may either be fossil (abandoned after
645 activation of the detachment) or reactivated by gravity-driven slip along the detachment.
646 Reactivation of the Himalayan suture along back-thrusts of post-early Oligocene age
647 [*Mascle et al.*, 1986; *Yin et al.*, 1994; *Aldsdorf et al.*, 1998] may indicate the emergence
648 of the retro fold-and-thrust belt produced experimentally.

649

650 *4. 3. Three-dimensional mass balance: transversal vs. longitudinal crustal flow*

651 The results of the two sets of experiments suggest that three-dimensional mass
652 redistribution takes place by combining transversal injection of plateau lower crust into
653 the frontal foreland as modeled by *Beaumont et al.* [2001], and lateral flow of the weak
654 lithosphere as proposed by *Royden et al.* [1997] (Figure 11). The relative magnitude of
655 the two processes is controlled by a balance between the degree of mechanical coupling
656 along the craton/plateau boundary and by lateral forces resulting from the resistance and
657 buoyancy of the lateral foreland. We observe that lateral escape observed in our 3D
658 experiments prevents significant continental underthrusting and concomitant injection
659 of plateau lower crust into the orogenic wedge. This implies that transversal
660 (injection/subduction) and longitudinal (escape) mass transfers may not coexist with
661 comparable fluxes during the entire evolution of the orogenic system. For an unstable
662 lithosphere, gravity forces can be accommodated by faulting in the upper crust and/or
663 by ductile flow at depth. Stages of transversal-dominated and escape-dominated flow
664 may alternate depending on the boundary conditions at the orogenic front and lateral
665 boundary. In the following, we propose a typical scenario for the three dimensional
666 evolution of a collision zone between a cratonic and a weak lithosphere.

667 The strength of the lateral foreland and forces arising from density contrasts on the
668 lateral boundary of the converging system primarily control the mode of lateral escape
669 of the weak lithosphere. As in our experiments, during the early stages of collision, a
670 weak lateral foreland and a large Argand number of the hot lithosphere enhance lateral
671 collapse-driven escape even for low values of shortening-induced thickening
672 (configuration of F2 experiment). A lateral flow regime is installed. In nature, lateral
673 escape could also be favored by lateral tension forces arising for instance from

674 subduction occurring close to the lateral boundary of the collision zone [e.g.,
675 *Tapponnier et al.*, 1986; *Ratschbacher et al.*, 1991b; *Fournier et al.*, 2004; *Schellart*
676 *and Lister*, 2005; *Faccenna et al.*, 2006]. Strength built-up in the lateral foreland as a
677 consequence of escape-driven tectonic thickening may reach a threshold, triggering
678 thickening of the weak lithosphere and slow forced tectonic extrusion (F1 experiment
679 configuration). At this stage, decoupling in the collision zone favors a transversal flow
680 regime driven by transformation of plateau overthickening into cratonward expulsion of
681 lower crust (Figures 4, 5 and 11).

682 The transversal flow regime is maintained as long as the stiff lateral foreland limits
683 collapse. During this period, gravity forces are accommodated by cratonward injection
684 of plateau lower crust between a thrust and a detachment, as the High Himalayan
685 Crystalline, whose exhumation was driven by coeval and opposed shearing along the
686 MCT and STD between ca. 25 and 13 Ma. In details, the exhumation process was
687 probably more complex, not fully synchronous along the range, and likely of lesser
688 amplitude than that simulated in *Beaumont et al.* [2004] and in our experiments,
689 especially considering the lateral structural / rheological heterogeneity of the lower crust
690 [*Long and McQuarrie*, 2010; *Rey et al.*, 2010; *Kellett and Grujic*, 2012].

691 A return to a lateral flow regime would be permitted if a change in the configuration
692 of the orogenic system would again permit collapse-driven lateral escape. Such a
693 change may result form a threshold in the gravitational potential of the weak lithosphere
694 with respect to its lateral foreland and/or from a drop in the degree of coupling at the
695 craton/plateau boundary. Such a process may have resulted from break-off of the Indian
696 subducting slab inferred to propagate from west to east between 25 and 10 Ma
697 [*Replumaz et al.*, 2010b; *Stearns et al.*, 2015]. Slab break-off may largely increase the
698 elevation of the plateau [e.g., *Molnar et al.*, 1993], its Argand number compared to its

699 lateral foreland and, in turn, favor lateral escape. The lateral flow regime would be
700 installed at the end of the break-off or once the process is completed. Initiation of a
701 subduction at the lateral boundary could also enhance lateral escape.
702 A reorganization of the frontal continental subduction fault system may also cause
703 for switching from a transversal to a lateral orogenic flow regime. Nucleation and
704 activation of a crustal ramp in the footwall of the transversally overflowing lower crust
705 (see above) could trigger an increase in the inter-plate coupling, an increase in
706 topography, and therefore favor collapse-driven lateral escape. Abandonment of the
707 MCT around 13 Ma and activation of the Main Boundary Thrust (MBT) could have
708 triggered such a change.
709 The switch from a transversal to a lateral orogenic flow regime is exemplified in the
710 Ama Drime Massif of the High Himalayan Crystalline, which has been exhumed at the
711 southern edge of the Tibetan plateau between the MCT and the STD. Exhumation of the
712 massif started at ca. 30 Ma along the STD with N-S extension, and the tectonic regime
713 then switched to E-W extension activating the NS-striking normal shear zones bounding
714 the massif at ca. 12-13 Ma [*Jessup et al.*, 2008; *Cottle et al.*, 2009; *Kali et al.*, 2010].
715 The age of ~ 13 Ma is consistent with the onset of lateral extension in the Tibetan
716 plateau estimated between 16 and 8 Ma [*Armijo et al.*, 1986; *Styron et al.*, 2015] and
717 attributed to lateral collapse [e.g., *Coleman and Hodges*, 1995; *Williams et al.*, 2001].
718 Lateral collapse therefore postdates the main episode of transversal flow of the High
719 Himalaya Crystalline between 25 and 15 Ma [*Burg et al.*, 1984; *Hubbard and Harrison*,
720 1989; *Hodges et al.*, 1992]. The formation of the MBT in the footwall of the MCT
721 around 13 – 12 Ma [e.g., *Kali et al.*, 2010] would have provided the necessary
722 conditions for a change from a transversal to longitudinal flow regime in the Himalaya-
723 Tibet orogenic system. This change may have been accompanied by a transient flow

724 regime during which the extruding lower crust of the High Himalaya Crystalline
725 recorded both transversal flow at depth and lateral flow at its roof [*Burg et al*., 1984;
726 *Brun et al.*, 1985; *Gapais et al.*, 1992; *Beaumont et al.*, 2001; *Murphy and Copeland*,
727 2005]. The onset of normal faulting is also documented at ca. 13 Ma in other Himalayan
728 domes [e.g. *Murphy et al.*, 2002; *Languille et al.*, 2014] and in Tibet [e.g. *Armijo et al.*,
729 1986; *Blisniuk et al.*, 2001; *Styron et al.*, 2015]. Rifts and extensional focal mechanisms
730 are more numerous in south than in central or north Tibet [*Copley et al.*, 2011]. We
731 propose that after 13 Ma, gravitational collapse was mainly accommodated by brittle
732 faulting in the upper crust in south Tibet and by ductile lateral flow in northern Tibet.
733 This can be understood considering that 1) lateral flow in south Tibet is partially
734 blocked by the east Himalayan syntaxis, 2) southern Tibet is underthrusted by India,
735 herewith increasing its overall strength. In our experiments, grabens are indeed more
736 developed in the plateau lithosphere for overall stronger ductile layers (Figures 6 and 7).
737 This would be consistent with recent studies highlighting the importance of India
738 underthrusting on rifting in Tibet [*Copley et al.*, 2011; *Ratschbacher et al.*, 2011; *Styron*
739 *et al.*, 2015]. If orogen-parallel extension is partly accommodated by brittle faulting in
740 northern Tibet, the main mechanism is ductile lateral flow along strike-slip faults, as in
741 our 3D experiments (Figure 6 to 8). In areas where the lithosphere has regained a stable
742 thickness, lateral escape could continue, driven by forced tectonic extrusion.
743

744 **5. Conclusions**

745 The present work suggests that paired orogenic plateaus – collisional wedges may
746 undergo two distinct syn-convergence flow regimes governed by the balance between
747 the gravity potential and the strength of the plateau crust, and the resistance of its lateral
748 foreland. A first possible regime, accretion dominated, is characterized by transversal

749 injection of plateau lower crust into the collisional wedge as a result of confinement of
750 the plateau by an increasingly stiffer lateral foreland. In this regime, transversal
751 injection is driven by downward thickening of the plateau crust that is forcedly extruded
752 into the orogenic wedge. The second orogenic flow regime is characterized by collapse-
753 driven lateral escape of the plateau as a consequence of increasing inter-plate coupling
754 in the collision zone, which increases the gravity potential of the plateau with respect to
755 the resistance of its lateral foreland. During collapse-driven lateral escape, a large
756 proportion of convergence-induced thickening of the plateau and the top of the
757 collisional wedge is transformed into lateral constrictional flow and extension.
758

759 **Acknowledgments**

760 This work was carried out at the experimental tectonic laboratory in Rennes. We
761 thank N. Durrieu, Y. Daoudene and M. Philippon for assistance in the lab and C.
762 Cavaré-Hester for finalizing figures 9 and 11. The paper benefited from a constructive
763 review by W. Schellart and an anonymous reviewer that helped improved an earlier
764 version of the manuscript.
765

766 **Appendix A. Calculation of the Argand number**

767 The Argand number allows the quantification of the stability of the lithosphere. It is
768 expressed as the ratio between body forces that favor the gravitational collapse of the
769 lithosphere, and tectonic forces that oppose it [*England and McKenzie*, 1982;
770 *Houseman and England*, 1986]:

771 $Ar = F_B/F_T$ (1)

For our models, the buoyancy force may be calculated as the difference between the gravitational potential energy of the lithosphere (cratonic or plateau type) integrated over depth and that of the lateral foreland (confining silicone)

$$F_B = \int^{z}_{surface} (\rho(z)\ z\ g)_{collision}\ dz - \int^{z}_{surface} (\rho(z)\ z\ g)_{lateral}\ dz \quad (2)$$

Given the collapse regime operating in the models with lateral escape, the tectonic force is calculated assuming a vertical σ_1 as the sum of tectonics forces necessary to stretch the brittle and ductile layers

$$F_T = F_{Tbrittle} + F_{Tductile} \quad (3)$$

with

$$F_{Tbrittle} = 1/3\ g\ \rho_{BC}\ h_{BC}^2 \quad (4)$$

$$F_{Tductile} = 2\ \eta\ h\ d\varepsilon/dt \quad (5)$$

where g is the gravity, ρ_{BC} and h_{BC} the density and thickness if the sand layer, η and h the viscosity and thickness of the silicone layer, and $d\varepsilon/dt$ the experimental strain rate. The strain rate $d\varepsilon/dt$ is calculated as

$$d\varepsilon/dt = V/W \quad (6)$$

where V is the shortening velocity and W the length of the model in the shortening-parallel direction. Thicknesses of layers at the end of each experiment were measured on the most internal and most external cross-sections; whereas those at the beginning of the experiments are known from model building. This allows us to quantify the stability of the lithospheres at the beginning and at the end of the experiments. Argand numbers are given in Table 4.

Appendix B. Quantification of deformation

796 Following the method proposed by *Cruden et al.* (2006), a three-dimensional finite
797 strain analysis has been performed by measuring deformation of the ductile layers on
798 each cross-section of the models. For this purpose, the x direction is defined as the
799 direction of convergence, y as the direction of lateral escape (orogen parallel), z as the
800 vertical direction. Initial and final measured lengths (L_0 and L) and thicknesses (T_0 and
801 T) of the ductile layers give the principal strains in x and z directions with the relation
802 $\lambda_x = (L/L_0)^2 = (1+\varepsilon_x)^2$ and $\lambda_z = (T/T_0)^2 = (1+\varepsilon_z)^2$ (1)
803 The principal strain in the direction of lateral escape (y) is calculated from the change in
804 cross-sectional area can be expressed as
805 $\lambda_y = (A_0/A)^2 = (1+\varepsilon_y)^2$ (2)
806 where A_0 and A are the initial and final area respectively. Flinn's K parameter defining
807 the aspect ratio of the strain ellispsoids has been calculated as
808 $K = (\lambda_1/\lambda_2-1)/(\lambda_2/\lambda_3-1)$ (3)
809 λ_1, λ_2 and λ_3 being the maximal, intermediate and minimum principal axes of the strain
810 ellipsoid, respectively. Strain intensity for each ellipsoid is estimated by ε_s [*Nadai*,
811 1950], defined as
812 $\varepsilon_s = (\sqrt{3})/2 * \gamma_0$ (4)
813 with
814 $\gamma_0 = 2/3 * \{[\ln(\lambda_1/\lambda_2)]^2+[\ln(\lambda_2/\lambda_3)]^2+[\ln(\lambda_3/\lambda_1)]^2\}^{1/2}$ (5)
815
816
817 **Note:** [1]. See supplementary material comprising photos, descriptions of the experiments
818 that were not detailed in the paper and tables containing strain and lateral escape
819 measurement data.
820

821 **References**

822 Alsdorf, D., L. Brown, K. D. Nelson, Y. Makovsky, S. Klemperer, and W. J. Zhao (1998),
823 Crustal deformation of the Lhasa terrane, Tibet plateau from Project INDEPTH deep
824 seismic reflection profiles, *Tectonics*, *17*(4), 501-519, doi:10.1029/98TC01315.
825 Andronicos, C. L., A. A. Velasco, and J. M. Hurtado (2007), Large-scale deformation in
826 the India-Asia collision constrained by earthquakes and topography, *Terra Nova*,
827 *19*, 105–119, doi:10.1111/j.1365-3121.2006.00714.x.
828 Armijo, R., P. Tapponnier, J. L. Mercier and H. Tong-Lin (1986), Quaternary extension
829 in Southern Tibet: Field observations and tectonic implications, *J. Geophys. Res.*,
830 *91*, B14, doi: 10.1029/JB091iB14p13803.
831 Bai, D. H., M. J. Unsworth, M. A. Meju, X. B. Ma, J. W. Teng, X. R. Kong, Y. Sun, L. F.
832 Wang, C. S. Jiang, C. P. Zhao, P. F. Xiao, and M. Liu (2010), Crustal deformation of the
833 eastern Tibetan plateau revealed by magnetotelluric imaging, *Nature Geoscience*, *3*(5),
834 358-362, doi:10.1038/Ngeo830.
835 Bajolet, F., A. Replumaz, and R. Laine (2013), Orocline and syntaxes formation during
836 subduction and collision, *Tectonics*, *32*(5), 1529-1546, doi:10.1002/Tect.20087.
837 Bao, X., X. Sun, M. Xu, Eaton D. W., X. Song, L. Wang, Z. Ding, N. Mi, H. Li, D. Yu, Z.
838 Huang, and P. Wang (2015), Two crustal low-velocity channels beneath SE Tibet revealed
839 by joint inversion of Rayleigh wave dispersion and receiver functions, *Earth Planet. Sci.*
840 *Lett.*, *415*, 16-24, doi:10.1016/j.epsl.2015.01.020.
841 Beaumont, C., R. A. Jamieson, M. H. Nguyen, and B. Lee (2001), Himalayan tectonics
842 explained by extrusion of a low-viscosity crustal channel coupled to focused surface
843 denudation, *Nature*, *414*, 738-742, doi:10.1038/414738a.
844 Beaumont, C., R. A. Jamieson, M. H. Nguyen, and S. Medvedev (2004), Crustal channel flows:
845 1. Numerical models with applications to the tectonics of the Himalayan-Tibetan orogen, *J.*

846 *Geophys. Res.*, *109*, B06406, doi:10.1029/2003JB002809.
847 Bird, P. (1991), Lateral Extrusion of Lower Crust from under High Topography, in the Isostatic
848 Limit, *J. Geophys. Res.*, *96*(B6), 10275-10286, doi: 10.1029/91JB00370.
849 Blisniuk, P. M., B. R. Hacker, J. Glodny, L. Ratschbacher, S. W. Bi, Z. H. Wu, M. O.
850 McWilliams, and A. Calvert (2001), Normal faulting in central Tibet since at least 13.5
851 Myr ago, *Nature*, *412*(6847), 628-632, doi:10.1038/35088045.
852 Brun, J. P., J. P. Burg, and C. G. Ming (1985), Strain Trajectories above the Main Central
853 Thrust (Himalaya) in Southern Tibet, *Nature*, *313*, 388-390, doi:10.1038/313388a0.
854 Brun, J. P. (2002), Deformation of the continental lithosphere: insights from brittle–ductile
855 model, in *Deformation Mechanisms, Rheology and Tectonics: Current Status and Future*
856 *Perspectives*, edited by S. De Meers, M. R. Drury, J. H. P. De Bresser and G. M. Pennock,
857 *Geol. Soc. Spec. Publ.*, *200*, 355-370, doi: 10.1144/GSL.SP.2001.200.01.20.
858 Burg, J. P., M. Brunel, D. Gapais, G. M. Chen, and G. H. Liu (1984), Deformation of
859 Leucogranites of the Crystalline Main Central Sheet in Southern Tibet (China), *J. Struct.*
860 *Geol.*, *6*(5), 535-542, doi:10.1016/0191-8141(84)90063-4.
861 Cagnard, F., N. Durrieu, D. Gapais, J. P. Brun, and C. Ehlers (2006a), Crustal thickening and
862 lateral flow during compression of hot lithospheres, with particular reference to
863 Precambrian times, *Terra Nova*, *18*(1), 72-78, doi: 10.1111/j.1365-3121.2005.00665.x.
864 Cagnard, F., J. P. Brun, and D. Gapais (2006b), Modes of thickening of analogue weak
865 lithospheres, *Tectonophysics*, *421*(1-2), 145-160, doi:10.1016/j.tecto.2006.04.016.
866 Chardon, D., D. Gapais, and F. Cagnard (2009), Flow of ultra-hot orogens: A view from the
867 Precambrian, clues for the Phanerozoic, *Tectonophysics*, *477*(3-4), 105-118,
868 doi:10.1016/j.tecto.2009.03.008.
869 Chardon, D., M. Jayananda, and J.•J. Peucat (2011), Lateral constrictional flow of hot
870 orogenic crust: Insights from the Neoarchean of south India, geological and

871 geophysical implications for orogenic plateaux, *Geochem. Geophys. Geosyst.*, *12*,
872 Q02005, doi:10.1029/2010GC003398.
873 Clark, M. K., K. A. Farley, D. W. Zheng, Z. C. Wang, and A. R. Duvall (2010), Early Cenozoic
874 faulting of the northern Tibetan Plateau margin from apatite (U-Th)/He ages, *Earth Planet.*
875 *Sci. Lett.*, *296*(1-2), 78-88, doi:10.1016/J.Epsl.2010.04.051.
876 Clark, M. K., and L. H. Royden (2000), Topographic ooze: Building the eastern margin of
877 Tibet by lower crustal flow, *Geology*, *28*(8), 703-706, doi:10.1130/0091-
878 7613(2000)28<703:TOBTEM>2.0.CO;2.
879 Coleman, M.E., and K.V. Hodges, 1995, Evidence for Tibetan plateau uplift before 14
880 m.y. ago from a new minimum age for east-west extension, *Nature*, *374*, 49–52,
881 doi:10.1038/374049a0.
882 Cook, K. L., and L. H. Royden (2008), The role of crustal strength variations in shaping
883 orogenic plateaus, with application to Tibet, *J. Geophys. Res.*, *113*(B8), B08407,
884 doi:10.1029/2007JB005457.
885 Copley, A., J. P. Avouac, and B. P. Wernicke (2011), Evidence for mechanical coupling and
886 strong Indian lower crust beneath southern Tibet, *Nature*, *472*(7341), 79-81,
887 doi:10.1038/Nature09926.
888 Cottle, J. M., M. J. Jessup, D. L. Newell, M. S. A. Horstwood, S. R. Noble, R. R. Parrish, D. J.
889 Waters, and M. P. Searle (2009), Geochronology of granulitized eclogite from the Ama
890 Drime Massif: Implications for the tectonic evolution of the South Tibetan Himalaya,
891 *Tectonics*, *28*, TC1002, doi:10.1029/2008TC002256.
892 Cruden, A. R., M. H. B. Nasseri, and R. Pysklywec (2006), Surface topography and
893 internal strain variation in wide hot orogens from three-dimensional analogue and
894 two-dimensional numerical vice models, in *Analogue and Numerical Modelling of*
895 *Crustal-Scale Processes*, edited by S. J. H. Buiter and G. Schreurs, *Geol. Soc. Spec.*

Publ., *253*, 79–104, doi:10.1144/GSL.SP.2006.253.01.04.

Davy, P., and Cobbold P. R. (1988), Indentation tectonics in nature and experiment, 1. Experiments scaled for gravity, *Bulletin of the Geological Institutions of Uppsala, New Series*, *14*, 129-141.

Davy, P., and P. R. Cobbold (1991), Experiments on Shortening of a 4-Layer Model of the Continental Lithosphere, *Tectonophysics*, *188*(1-2), 1-25, doi:10.1016/0040-1951(91)90311-F.

Dewey, J.F. (1988), Extensional collapse or orogens, *Tectonics, 7*(6), 1123-1139, doi:10.1029/TC007i006p01123.

Duretz, T., B. J. P. Kaus, K. Schulmann, D. Gapais, and J.-J. Kermarrec (2011), Indentation as an extrusion mechanism of lower crustal rocks: Insight from analogue and numerical modelling, application to the Eastern Bohemian Massif, *Lithos*, *124*(1-2), 158-168, doi:10.1016/j.lithos.2020.10.013.

England, P., and G. Houseman (1989), Extension during Continental Convergence, with Application to the Tibetan Plateau, *J. Geophys. Res.*, *94*(B12), 17,561-17,579, doi:10.1029/JB094iB12p17561.

England, P., and D. McKenzie (1982), A thin viscous sheet model for continental deformation, *Geophys. J. R. Astron. Soc.*, *70*, 295–321, doi:10.1111/j.1365-246X.1982.tb04969.x.

England, P. C., and A. B. Thompson (1984), Pressure temperature time paths of regional metamorphism. 1. Heat transfer during the evolution of regions of thickened continental crust, *J. Petrol.*, *25*(4), 894–928, doi:10.1093/petrology/25.4.894.

Faccenna, C., O. Bellier, J. Martinod, C. Piromallo and V. Regard (2006), Slab detachment beneath eastern Anatolia: A possible cause for the formation of the

North Anatolian fault, *Earth Planet. Sci. Lett.*, *242*, 85-97, doi: 10.1016/j.epsl.2005.11.046.

Fournier, M., L. Jolivet, P., Davy, J. C., Thomas, (2004), Backarc extension and collision: an experimental approach to the tectonics of Asia, *Geoph. J. Int.*, *157*(2), 871-889, doi: 10.1111/j.1365-246X.2004.02223.x.

Gapais, D., A. Pêcher, E. Gilbert, and M. Ballevre (1992), Synconvergence Spreading of the Higher Himalaya Crystalline in Ladakh, *Tectonics, 11*(5), 1045-1056, doi: 10.1029/92TC00819.

Godin, L., C. Yakymchuk, and L. B. Harris (2011), Himalayan hinterland-verging superstructure folds related to foreland-directed infrastructure ductile flow: Insights from centrifuge analogue modelling, *J. Struct. Geol.*, *33*(3), 329-342, doi:10.1016/J.Jsg.2010.09.005.

Grujic, D., M. Casey, C. Davidson, L. S. Hollister, R. Kundig, T. Pavlis, and S. Schmid (1996), Ductile extrusion of the Higher Himalayan Crystalline in Bhutan: Evidence from quartz microfabrics, *Tectonophysics*, 260(1-3), 21-43, doi:10.1016/0040-1951(96)00074-1.

Hodges, K. V., R. R. Parrish, T. B. Housh, D. R. Lux, B. C. Burchfiel, L. H. Royden, and Z. Chen (1992), Simultaneous Miocene Extension and Shortening in the Himalayan Orogen, *Science*, *258*, 1,466-1,470, doi:10.1126/science.258.5087.1466.

Holt, W. E. (2000), Correlated crust and mantle strain fields in Tibet, *Geology*, *28*, 67–70, doi:10.1130/0091-7613(2000)28<67:CCAMSF>2.0.CO;2.

Houseman, G., and P. England (1986), Finite strain calculations of continental deformation 1. Method and general results for convergent zones. *J. Geophys. Res.*, *91*(B3), 3,651–3,663, doi:10.1029/JB091iB03p03651.

Hubbard, M. S., and T. M. Harrison (1989), Ar-40/Ar-39 Age Constraints on Deformation and Metamorphism in the Main Central Thrust Zone and Tibetan Slab, Eastern Nepal

946 Himalaya, *Tectonics*, *8*(4), 865-880, doi:10.1029/TC008i004p00865.
947 Jessup, M. J., D. L. Newell, J. M. Cottle, A. L. Berger, and J. A. Spotila (2008), Orogen-
948 parallel extension and exhumation enhanced by denudation in the trans-Himalayan Arun
949 River gorge, Ama Drime Massif, Tibet-Nepal, *Geology*, *36*(7), 587-590,
950 doi:10.1130/G24722A.1.
951 Jimenez-Munt, I., M., Fernandez, J., Verges, J. P., Platt (2008), Lithosphere structure
952 underneath the Tibetan Plateau inferred from elevation, gravity and geoid
953 anomalies, *Earth Planet. Sci. Lett.*, *267*(1-2), 276-289,
954 doi:10.1016/j.epsl.2007.11.045.
955 Kali, E., P. H. Leloup, N. Arnaud, G. Maheo, D. Y. Liu, E. Boutonnet, J. Van der
956 Woerd, X. H. Liu, L. Z. Jing, and H. B. Li (2010), Exhumation history of the
957 deepest central Himalayan rocks, Ama Drime range: Key pressure-temperature-
958 deformation-time constraints on orogenic models, *Tectonics*, *29*, TC2014,
959 doi:10.1029/2009TC002551.
960 Kapp, P., and J. H. Guynn (2004), Indian punch rifts Tibet, *Geology*, *32*(11), 993-996,
961 doi:10.1130/G20689.1.
962 Kellett, D. A., and D. Grujic (2012), New insight into the South Tibetan detachment system:
963 Not a single progressive deformation, *Tectonics*, *31*, TC2007, doi:10.1029/2011tc002957.
964 Langille, J. M., M. J. Jessup, J. Cottle, and T. Ahmad (2014), Kinematic and thermal studies of
965 the Leo Pargil Dome: Implications for synconvergent extension in the NW Indian
966 Himalaya, *Tectonics*, *33*(9), 1766-1786, doi:10.1002/2014tc003593.
967 Li, C., R. D. Van der Hilst, A. S. Meltzer, and E. R. Engdahl (2008), Subduction of the
968 Indian lithosphere beneath the Tibetan Plateau and Burma, *Earth Planet. Sci. Lett.*,
969 *274*(1-2), 157-168, doi:10.1016/j.epsl.2008.07.016.
970 Liu, Q. Y., R. D. van der Hilst, Y. Li, H. J. Yao, J. H. Chen, B. Guo, S. H. Qi, J. Wang, H.

971 Huang, and S. C. Li (2014), Eastward expansion of the Tibetan Plateau by crustal flow and
972 strain partitioning across faults, *Nature Geoscience*, *7*(5), 361-365, doi:10.1038/Ngeo2130.
973 Lohrmann, J., N. Kukowski, J. Adam, and O. Oncken (2003), The impact of analogue material
974 properties on the geometry, kinematics, and dynamics of convergent sand wedges, *J.*
975 *Struct. Geol.*, *25*(10), 1691-1711, doi:Pii S0191-8141(03)00005-1
976 Loiselet, C., L. Husson and J. Braun (2009), From longitudinal slab curvature to slab
977 rheology, *Geology*, *37*(8), 747-750, doi:10.1130/G30052A.
978 Long, S., and N. McQuarrie (2010), Placing limits on channel flow: Insights from the Bhutan
979 Himalaya, *Earth Planet Sci. Lett.*, *290*(3-4), 375-390, doi:10.1016/J.Epsl.2009.12.033.
980 Mascle, G., G. Hérail, T. Van Haver, and B. Delcaillau (1986), Structure et évolution
981 des basins d'épisuture et de périsuture lies à la chaîne himalayenne, *Bull. Centre*
982 *Rech. Explor.-Prod. Elf Aquitaine*, *10*, 182-203.
983 Merle, O. and B. Guillier (1989), The building of the Central Swiss Alps: an
984 experimental approach, *Tectonophysics*, *165*, 41-56, doi:10.1016/0040-
985 1951(89)90034-6.
986 Merle, O. and D. Gapais (1997), Strains within thrust-wrench zones, *J. Struct. Geol.*,
987 *19*(7), 1011-1014, doi:10.1016/S0191-8141(97)00027-8.
988 Molnar, P., P. England, and J. Martinod (1993), Mantle Dynamics, Uplift of the Tibetan
989 Plateau, and the Indian Monsoon, *Reviews of Geophysics*, *31*(4), 357-396,
990 doi:10.1029/93RG02030.
991 Murphy, M. A., A. Yin, P. Kapp, T. M. Harrison, C. E. Manning, F. J. Ryerson, L. Ding, and J.
992 H. Guo (2002), Structural evolution of the Gurla Mandhata detachment system, southwest
993 Tibet: Implications for the eastward extent of the Karakoram fault system, *Geol. Soc. Am.*
994 *Bull.*, *114*(4), 428-447, doi:10.1130/0016-7606(2002)114<0428:Seotgm>2.0.Co;2.

995 Murphy, M. A., and P. Copeland (2005), Transtensional deformation in the central
996 Himalaya and its role in accommodating growth of the Himalayan orogen,
997 *Tectonics*, *24*, TC4012, doi:10.1029/2004TC001659.
998 Murphy, M. A., V. Sanchez, and M. H. Taylor (2010), Syncollisional extension along the
999 India-Asia suture zone, south-central Tibet: Implications for crustal deformation of Tibet,
1000 *Earth Planet. Sci. Lett.*, *290*(3-4), 233-243, doi:10.1016/J.Epsl.2009.11.046.
1001 Nadai, A. (1950), *Theory of Flow and Fracture of Solids*, McGraw-Hill, New York, 705
1002 pp.
1003 Priestley, K., J. Jackson, and D. McKenzie (2007), Lithospheric structure and deep earthquakes
1004 beneath India, the Himalaya and southern Tibet, *Geophys. J. Int.*, *172*(1), 345-362,
1005 doi:10.1111/j.1365-246X.2007.03636.x.
1006 Ratschbacher, L., O. Merle, P. Davy, and P. Cobbold (1991a), Lateral extrusion in the eastern
1007 Alps, part 1: Boundary conditions and experiments scaled for gravity, *Tectonics, 10*(2),
1008 245-256, doi:10.1029/90TC02622.
1009 Ratschbacher, L., W. Frisch, H-G. Linzer and O. Merle (1991b), Lateral extrusion in the
1010 eastern Alps, part 2: Structural analysis, *Tectonics, 10*(2), 257-271,
1011 doi:10.1029/90TC02623.
1012 Ratschbacher, L., W. Frisch, G. H. Liu, and C. S. Chen (1994), Distributed Deformation in
1013 Southern and Western Tibet during and after the India-Asia Collision, *J. Geophys. Res.*,
1014 *99*(B10), 19917-19945, doi:10.1029/94jb00932.
1015 Ratschbacher, L., I. Krumrei, M. Blumenwitz, M. Staiger, R. Gloaguen, B. V. Miller, S. D.
1016 Samson, M. A. Edwards, and E. Appel (2011), Rifting and strike-slip shear in central Tibet
1017 and the geometry, age and kinematics of upper crustal extension in Tibet, in *Growth and*
1018 *Collapse of the Tibetan Plateau*, edited by Gloaguen, R., and L. Ratschbacher, *Geol. Soc.*
1019 *Spec. Publ., 353*, 127-163, doi:10.1144/SP353.8.

1020 Replumaz, A., A. M. Negredo, S. Guillot, P. van der Beek, and A. Villasenor (2010c),
1021 Crustal mass budget and recycling during the India/Asia collision, *Tectonophysics*,
1022 *492*(1-4), 99-107, doi:10.1016/j.tecto.2010.05.023.
1023 Replumaz, A., A. M. Negredo, A. Villasenor, and S. Guillot (2010b), Indian continental
1024 subduction and slab break-off during Tertiary Collision, *Terra Nova*, *22*(4), 290-296,
1025 doi:10.1111/j.1365-3121.2010.00945.x.
1026 Rey, P. F., C. Teyssier, and D. L. Whitney (2010), Limit of channel flow in orogenic plateaux,
1027 *Lithosphere*, *2*(5), 328-332, doi:10.1130/L114.1.
1028 Riller, U., A. R. Cruden, D. Boutelier, and C. E. Schrank (2012), The causes of sinuous
1029 crustal-scale deformation patterns in hot orogens: Evidence from scaled analogue
1030 experiments and the southern Central Andes, *J. Struct. Geol.*, *37*, 65-74,
1031 doi:10.1016/j.jsg.2012.02.002.
1032 Robert, A., M. Pubellier, J. de Sigoyer, J. Vergne, A. Lahfid, R. Cattin, N. Findling, and J. Zhu
1033 (2010), Structural and thermal characters of the Longmen Shan (Sichuan, China),
1034 *Tectonophysics*, *491*(1-4), 165-173, doi:10.1016/J.Tecto.2010.03.018.
1035 Royden, L. (1996), Coupling and decoupling of crust and mantle in convergent orogens:
1036 Implications for strain partitioning in the crust, *J. Geophys. Res.*, *101*(B8), 17,679-17,705,
1037 doi:10.1029/96JB00951.
1038 Royden, L. H., B. C. Burchfiel, R. W. King, E. Wang, Z. L. Chen, F. Shen, and Y. P. Liu
1039 (1997), Surface deformation and lower crustal flow in eastern Tibet, *Science*, *276*(5313),
1040 788-790, doi:10.1126/science.276.5313.788.
1041 Royden, L. H., B. C. Burchfiel, and R. D. van der Hilst (2008), The Geological Evolution of
1042 the Tibetan Plateau, *Science, 321*, 1054-1058, doi:10.1126/science.1155371.

1043 Sandiford, M., and R. Powell (1991), Some remarks on high temperature•low•pressure
1044 metamorphism in convergent orogens, *J. Metamorph. Geol.*, *9*, 333–340,
1045 doi:10.1111/j.1525-1314.1991.tb00527.x.
1046 Schellart, W. P. (2000), Shear test results for cohesion and friction coefficients for different
1047 granular materials: scaling implications for their usage in analogue modelling,
1048 *Tectonophysics*, *324*(1-2), 1-16, doi:10.1016/S0040-1951(00)00111-6.
1049 Schellart, W. P. (2010), Evolution of Subduction Zone Curvature and its Dependence on the
1050 Trench Velocity and the Slab to Upper Mantle Viscosity Ratio, *J. Geoph. Res.*, *115*,
1051 B11406, doi:10.1029/2009JB006643.
1052 Schellart, W. P., and G. S. Lister (2005), The role of the East Asian active margin in
1053 widespread extensional and strike-slip deformation in East Asia, *J. Geol. Soc.*, *162*, 959-
1054 972, doi:10.1144/0016-764904-112.
1055 Searle, M. P., J. R. Elliott, R. J. Phillips, and S. L. Chung (2011), Crustal-lithospheric structure
1056 and continental extrusion of Tibet, *J. Geol. Soc. London*, *168*(3), 633-672,
1057 doi:10.1144/0016-76492010-139.
1058 Seeber, L., and A. Pecher (1998), Strain partitioning along the Himalayan arc and the Nanga
1059 Parbat antiform, *Geology*, *26*(9), 791-794, doi:10.1130/0091-
1060 7613(1998)026<0791:Spatha>2.3.Co;2.
1061 Shen, F., L. H. Royden, and B. C. Burchfiel (2001), Large-scale crustal deformation of the
1062 Tibetan Plateau, *J. Geophys. Res.*, *106*(B4), 6793-6816, doi:10.1029/2000jb900389.
1063 Steck, L. K., A. A. Velasco, A. H. Cogbill, and H. J. Patton (2001), Improving regional seismic
1064 event location in China, *Pure App. Geoph.*, *158*(1-2), 211-240, doi:10.1007/Pl00001157.
1065 Stearns, M. A., B. R. Hacker, Ratschbacher L., Rutte D., and A. R. C. Kylander-Clark (2015),
1066 Titanite petrochronology of the Pamir gneiss domes: Implications for middle to deep crust
1067 exhumation and titanite closure to Pb and Zr diffusion, *Tectonics*, 34, 784-802,

doi:10.1002/2014TC003774.

Styron, R., M. Taylor, and K. Sundell (2015), Accelerated extension of Tibet linked to the northward underthrusting of Indian crust, *Nature Geoscience*, *8*, 131-134, doi:10.1038/NGEO2336.

Tapponnier, P., G. Peltzer, A. Y. La Dain, R. Armijo, and P. Cobbold (1982), Propagating extrusion tectonics in Asia: New insights from simple experiments with plasticine, *Geology*, *10*, 611-616, doi:10.1130/0091-7613(1982)10<611:PETIAN>2.0.CO;2.

Tapponnier, P., G. Peltzer, and R. Armijo (1986), On the mechanics of the collision between India and Asia, *Geol. Soc. London Spec. Publ.*, 19, 113-157.

Tapponnier, P., Z. Q. Xu, F. Roger, B. Meyer, N. Arnaud, G. Wittlinger, and J. S. Yang (2001), Geology - Oblique stepwise rise and growth of the Tibet plateau, *Science*, *294*(5547), 1671-1677, doi:10.1126/Science.105978.

Taylor, M., A. Yin, F. J. Ryerson, P. Kapp, and L. Ding (2003), Conjugate strike-slip faulting along the Bangong-Nujiang suture zone accommodates coeval east-west extension and north-south shortening in the interior of the Tibetan Plateau, *Tectonics*, *22*(4), 1044, doi:10.1029/2002tc001361.

Teyssier, C. and B. Tikoff (1999), Fabric stability in oblique convergence and divergence, *J. Struct. Geol.*, *21*(8-9), 969-974, doi:10.1016/S0191-8141(99)00067-X.

Tikoff, B., R. Russo, C. Teyssier, and A. Tommasi (2004), Mantle-driven deformation of orogenic zones and clutch tectonic, in *Vertical Coupling and Uncoupling in the Lithosphere*, edited by Grocott, J., K.J.W. McCaffrey, G. Taylor, and B. Tikoff, *Geol. Soc. Spec. Publ.*, *227*, 41-64, doi:10.1144/GSL.SP.2004.227.01.03.

Vanderhaeghe, O., and C. Teyssier (2001), Partial melting and flow of orogens,

Tectonophysics, *342*(3-4), 451-472, doi:10.1016/S0040-1951(01)00175-5.

Weijermars, R., and H. Schmeling (1986), Scaling of Newtonian and non-Newtonian fluid dynamics without inertia for quantitative modeling of rock flow due to gravity (including the concept of rheological similarity), *Phys. Earth Planet. Int.*, *43*, 316-330, doi:10.1016/0031-9201(86)90021-X.

Williams, H., S. Turner, S. Kelley, and N. Harris (2001), Age and composition of dikes in Southern Tibet: New constraints on the timing of east-west extension and its relationship to postcollisional volcanism, *Geology*, *29*(4), 339–342, doi:10.1130/0091-7613(2001)029<0339:AACODI>2.0.CO;2.

Yin, A., T.M. Harrison, F.J. Ryerson, C. Wenji, W.S.F. Kidd, and P. Copeland (1994), Tertiary structural evolution of the Gangdese thrust system, southeastern Tibet, *J. Geophys. Res.*, *99*, 18,175-18,201, doi:10.1029/94JB00504.

Zhang, P. Z., Z. Shen, M. Wang, W. J. Gan, R. Burgmann, and P. Molnar (2004), Continuous deformation of the Tibetan Plateau from global positioning system data, *Geology*, *32*(9), 809-812, doi:10.1130/G20554.1.

Table captions

Table 1. Experimental parameters.

Table 2. Material properties for experiments laterally confined and with lateral escape.

Table 3. Differential stress of the ductile lithospheric layers for two different experimental shortening rates.

Table 4. Strain intensities (ε_s) and Argand numbers (Ar) calculated for experiments with lateral escape. Argand numbers are given for initial and final configurations for the most internal and external parts of the models. For experiment F1, lack of cross-sections did not allow us to calculate the final Ar and ε_s.

Figure captions

Figure 1. a) Map of the main tectonic features of the Tibet-Himalaya orogenic system. Grabens and detachment faults are highlighted in red. F: fault; BNS: Bangong-Nujiang Suture; IT: Indus-Tsangpo; STD: South-Tibetan detachment; MCT: Main Central Thrust; MBT: Main Boundary Thrust; MFT: Main Frontal Thrust; LMSF: Longmenshan fault.
b) Synthetic cross-section. BC: brittle crust; WLC: weak lower crust; CLM: cratonic lithospheric mantle.

Figure 2. Experimental setup. The graphs are strength profiles of both types of lithospheres. BC: brittle crust; DC: ductile crust; WLC: weak lithosphere lower crust; CLM: cratonic lithospheric mantle. Strength values are given in Table 3.

Figure 3. Top views and cross-sections of experiment C1 (see Tables 1 and 2 for parameters). Top views (top) show selected stages of fault surface pattern development, that on the right showing the configuration at the end of the experiment. On cross-sections, the numbers and percentages in bracket refer to the order of appearance and amount of shortening at which each fault formed, respectively. The lines of sections (5, 3) are located on the last top view. WL: weak lithosphere; CL: cratonic lithosphere; d: dome (see text).

Figure 4. Cross-sections of experiments C2, C4, C5, C6, C7 and C8 (see Tables 1 and 2 for parameters). White dashed lines represent originally horizontal passive markers in the ductile layers. Ductile lower crust in the weak lithosphere of experiments C7 and C8

(TWLC in Tables 1 and 2) is initially doubly thickened. In experiment C7 (panel 4e), the markers slightly lighter than the DC tend to localize the deformation. Moreover, the model is deformed by post-experiment downwarping. See Figure 3 for caption.

Figure 5. Top views and cross-sections of experiment C3 (see Tables 1 and 2 for parameters). White dashed lines represent passive markers in the ductile layers that were originally horizontal. See Figure 3 for caption.

Figure 6. Top views and cross-sections of experiment F2 (see Tables 1 and 2 for parameters, and Figure 3 for caption).

Figure 7. Top views and cross-sections of experiment F3 (see Tables 1 and 2 for parameters, and Figure 3 for caption).

Figure 8. Top views of experiment F1 (see Tables 1 and 2 for parameters).

Figure 9. Summary of results of experiments with lateral escape. See text for further explanations.

Figure 10. Relationships between lateral escape, thickening and thinning through time for experiments with lateral escape. (a) to (c) Lateral escape of the model lithospheres through time based on top view analysis. The portion of the area lost by the advancing piston that is absorbed by lithospheric thickening results from the subtraction of the total lithospheric area escaped to the area lost by advancing piston. (d) Evolution of the thickening/escape ratio versus shortening.

1176

1177 **Figure 11.** Idealized view of two-stage orogenic flow mode at the edge of an orogenic

1178 plateau. See text for further explanations.

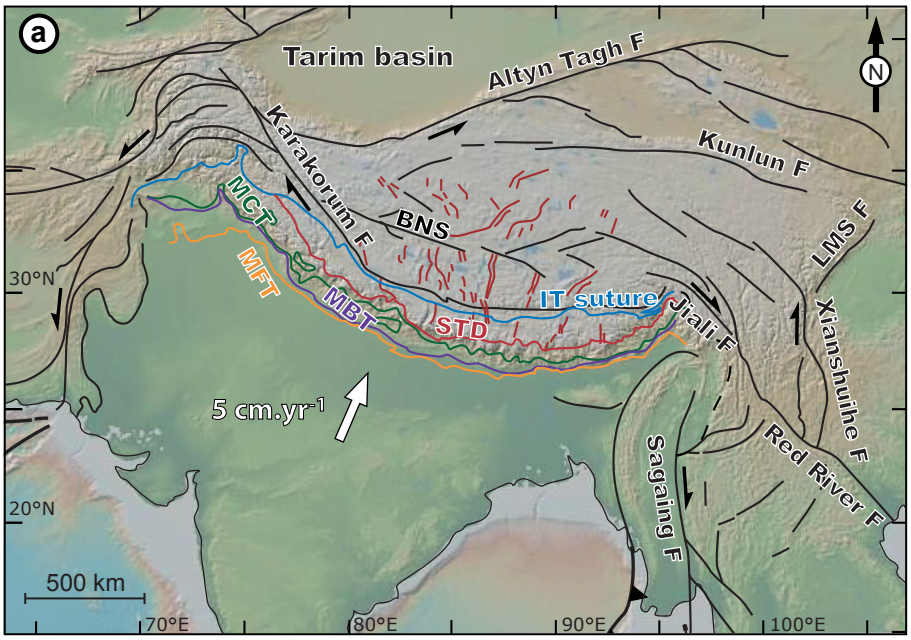
a
Tarim basin
Altyn Tagh F
Karakorum F
Kunlun F
BNS
MCT
MFT
MBT
STD
IT suture
Jiali F
LMS F
Xianshuihe F
Red River F
Sagaing F
5 cm.yr-1
N
30°N
20°N
500 km
70°E
80°E
90°E
100°E

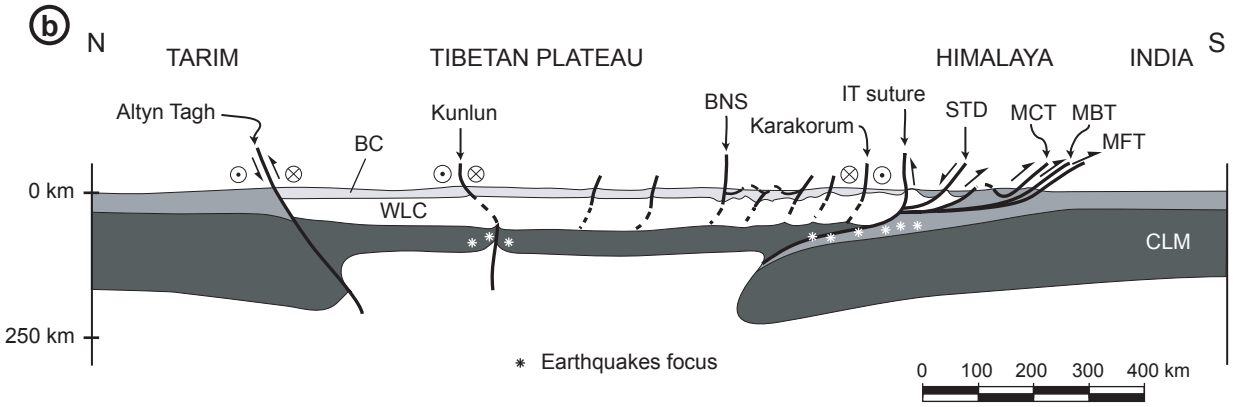
b
N
S
TARIM
TIBETAN PLATEAU
HIMALAYA
INDIA
Altyn Tagh
BC
Kunlun
BNS
Karakorum
IT suture
STD
MCT
MBT
MFT
0 km
WLC
CLM
250 km
Earthquakes focus
0
100
200
300
400 km

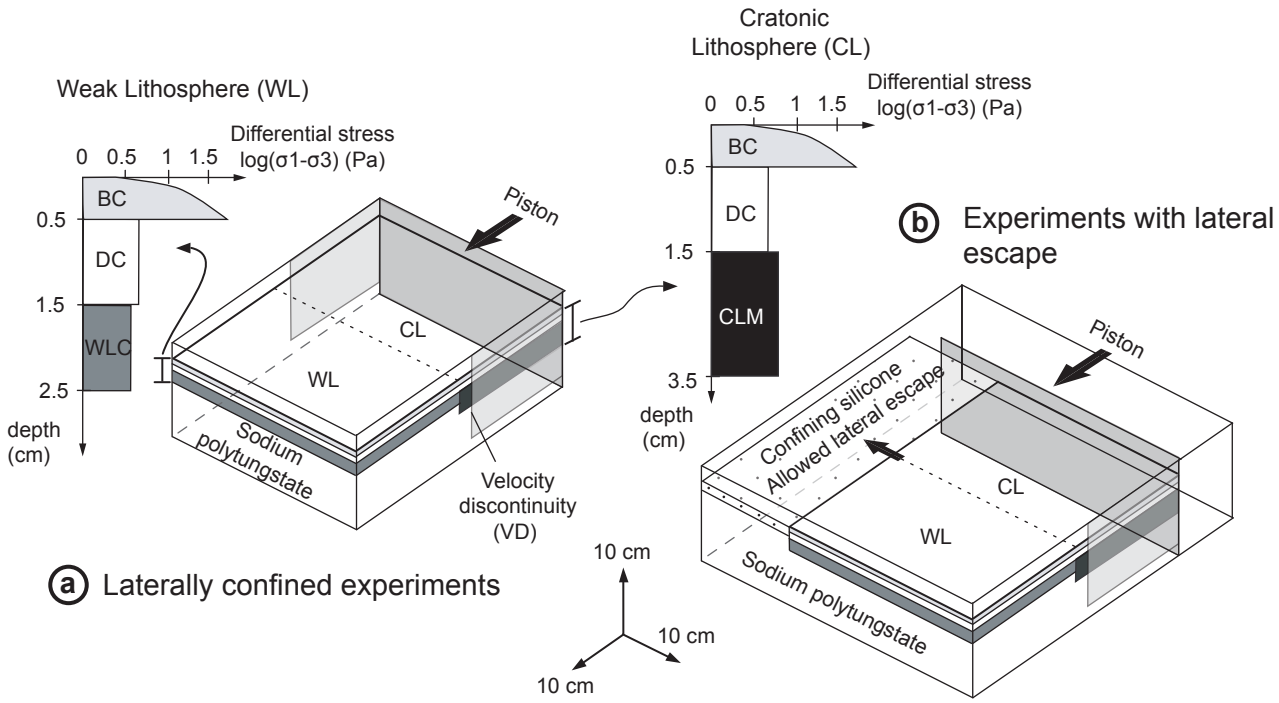

(a) Laterally confined experiments

(b) Experiments with lateral escape

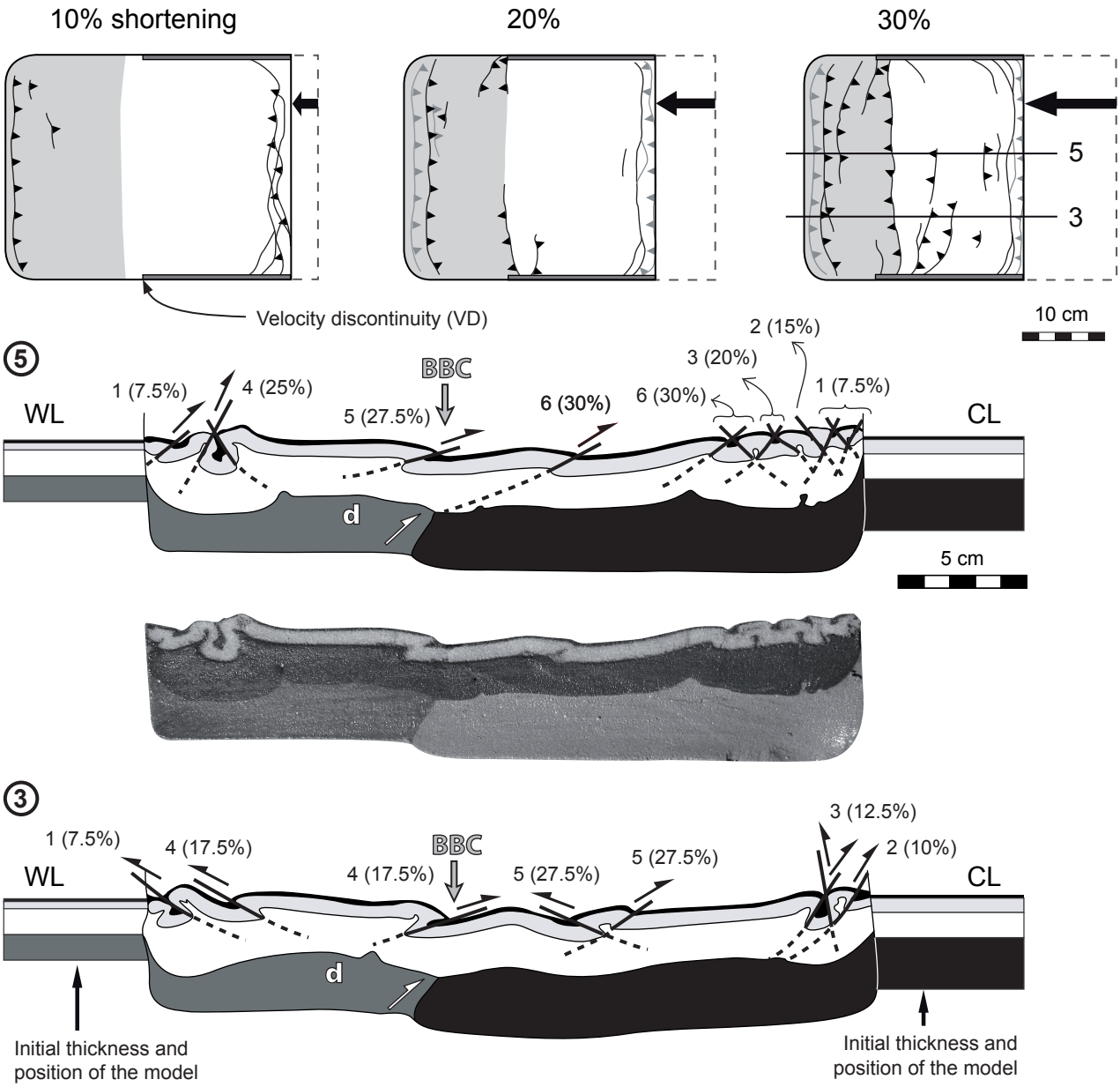

Cross-section view

- Brittle crust
- Ductile crust (DC)
- Weak lower crust (WLC)
- Cratonic lithospheric mantle (CLM)
- Shear sense
- BBC — Boundary between WL and CL brittle crusts
- Passive markers in ductile crust
- Neutral silicone
- Thickened weak lower crust (TWLC)
- Thrust fault
- Normal fault
- Indentation

Plane view

- Fault
- Thrust fault: active / abandonned
- Normal fault: active / abandonned
- Strike-slip fault
- Weak lithosphere brittle crust

C1 settings:

- laterally confined
- 30% shortening
- 2cm/h
- homogeneous sand thickness

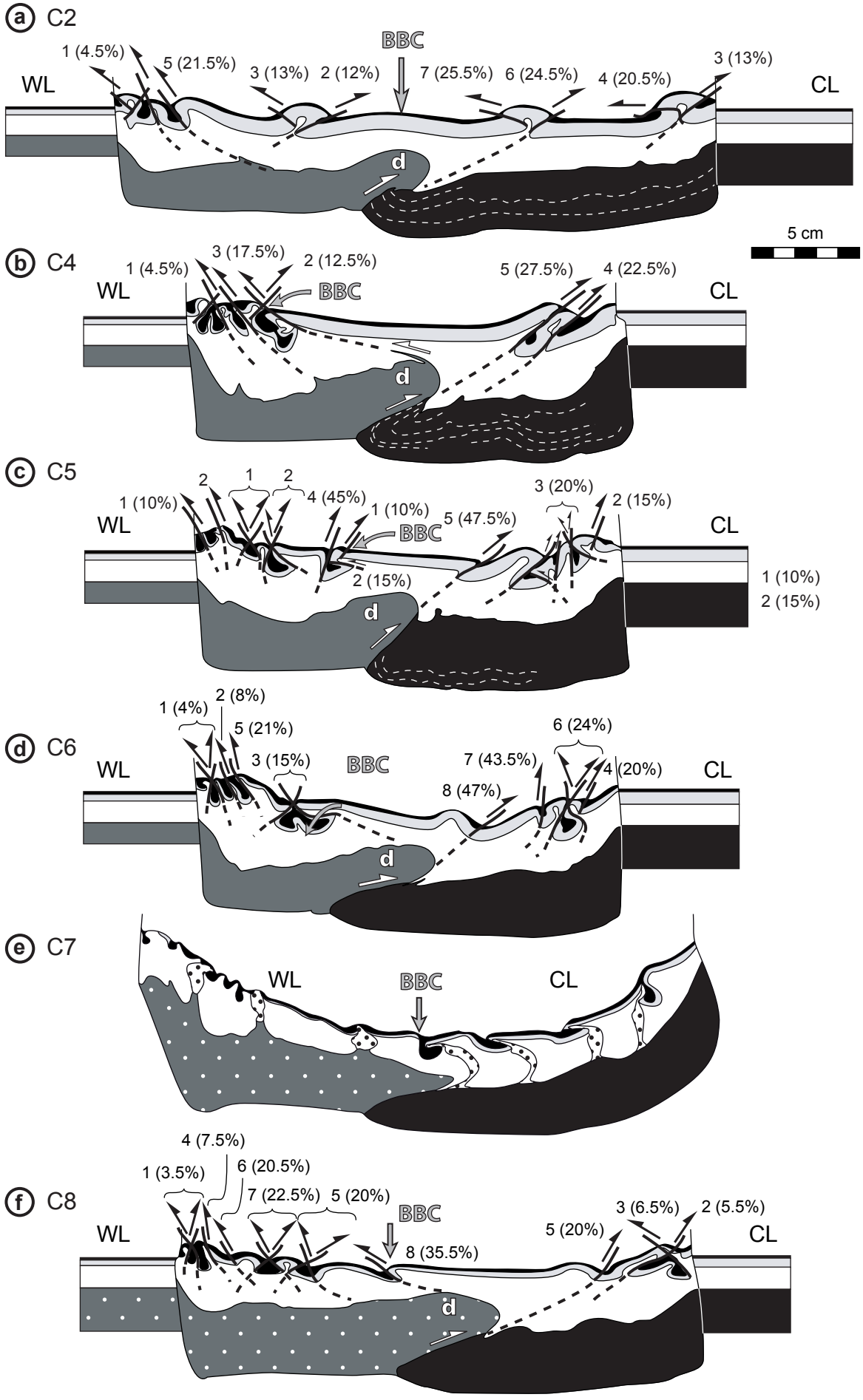
a C2
BBC
1 (4.5%)
5 (21.5%)
3 (13%)
2 (12%)
7 (25.5%)
6 (24.5%)
4 (20.5%)
3 (13%)
WL
CL
d
5 cm
b C4
3 (17.5%)
1 (4.5%)
2 (12.5%)
5 (27.5%)
4 (22.5%)
BBC
WL
CL
d
c C5
2
1
2
1 (10%)
4 (45%)
1 (10%)
5 (47.5%)
3 (20%)
2 (15%)
BBC
WL
CL
2 (15%)
1 (10%)
2 (15%)
d
d C6
1 (4%)
2 (8%)
5 (21%)
6 (24%)
3 (15%)
BBC
7 (43.5%)
4 (20%)
8 (47%)
WL
CL
d
e C7
WL
BBC
CL
f C8
4 (7.5%)
1 (3.5%)
6 (20.5%)
7 (22.5%)
5 (20%)
BBC
3 (6.5%)
2 (5.5%)
5 (20%)
8 (35.5%)
WL
CL
d

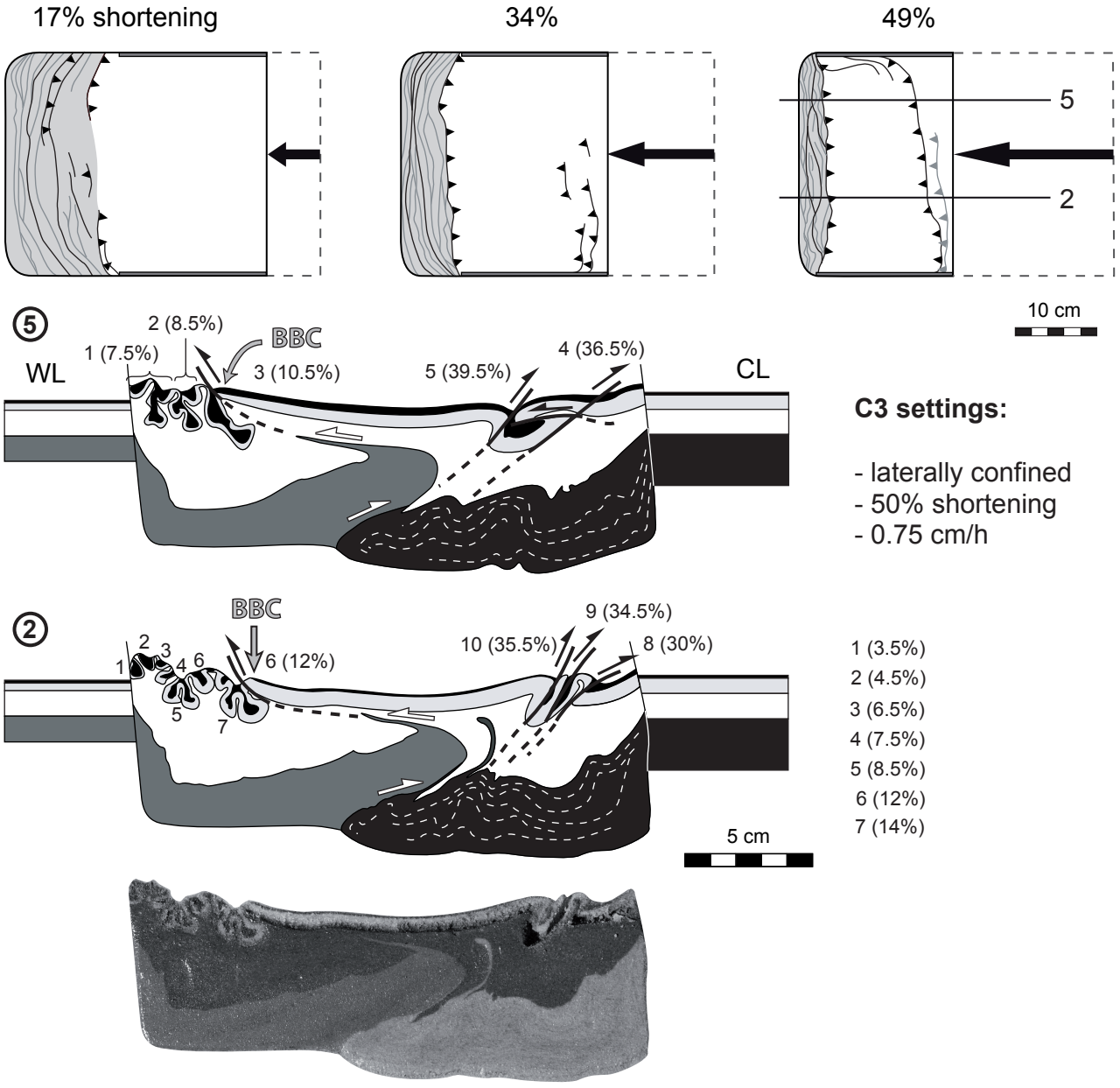
17% shortening
34%
49%
5
2
10 cm
⑤
2 (8.5%)
1 (7.5%)
BBC
3 (10.5%)
WL
5 (39.5%)
4 (36.5%)
CL
C3 settings:
- laterally confined
- 50% shortening
- 0.75 cm/h
②
BBC
9 (34.5%)
10 (35.5%)
8 (30%)
2
3
1
4
6
6 (12%)
5
7
1 (3.5%)
2 (4.5%)
3 (6.5%)
4 (7.5%)
5 (8.5%)
6 (12%)
7 (14%)
5 cm

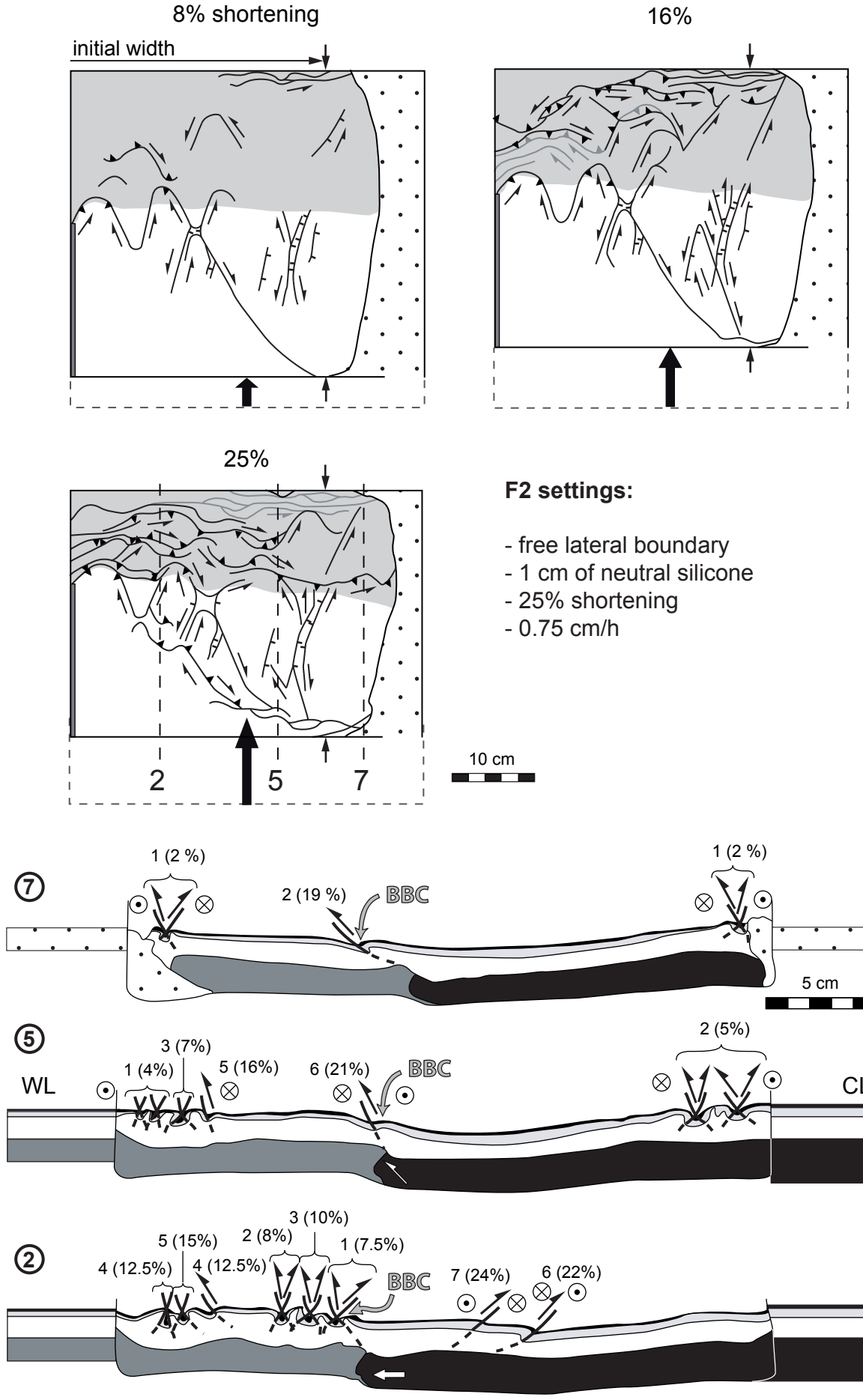
8% shortening
initial width
16%
25%
2
5
7
10 cm
F2 settings:
- free lateral boundary
- 1 cm of neutral silicone
- 25% shortening
- 0.75 cm/h
⑦
1 (2 %)
2 (19 %)
BBC
1 (2 %)
5 cm
⑤
WL
3 (7%)
1 (4%)
5 (16%)
6 (21%)
BBC
2 (5%)
CL
②
5 (15%)
4 (12.5%)
4 (12.5%)
2 (8%)
3 (10%)
1 (7.5%)
BBC
7 (24%)
6 (22%)

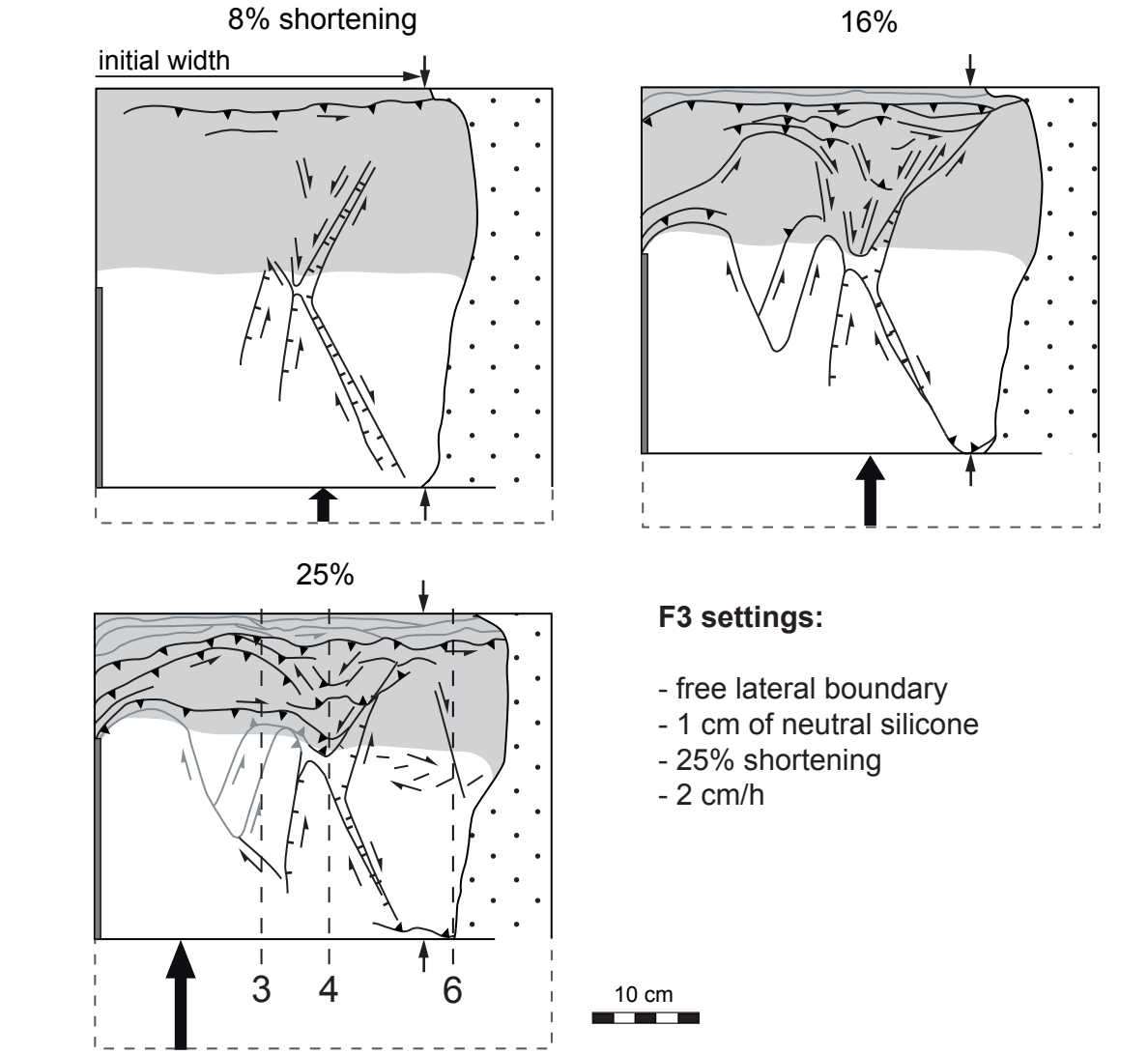

F3 settings:

- free lateral boundary
- 1 cm of neutral silicone
- 25% shortening
- 2 cm/h

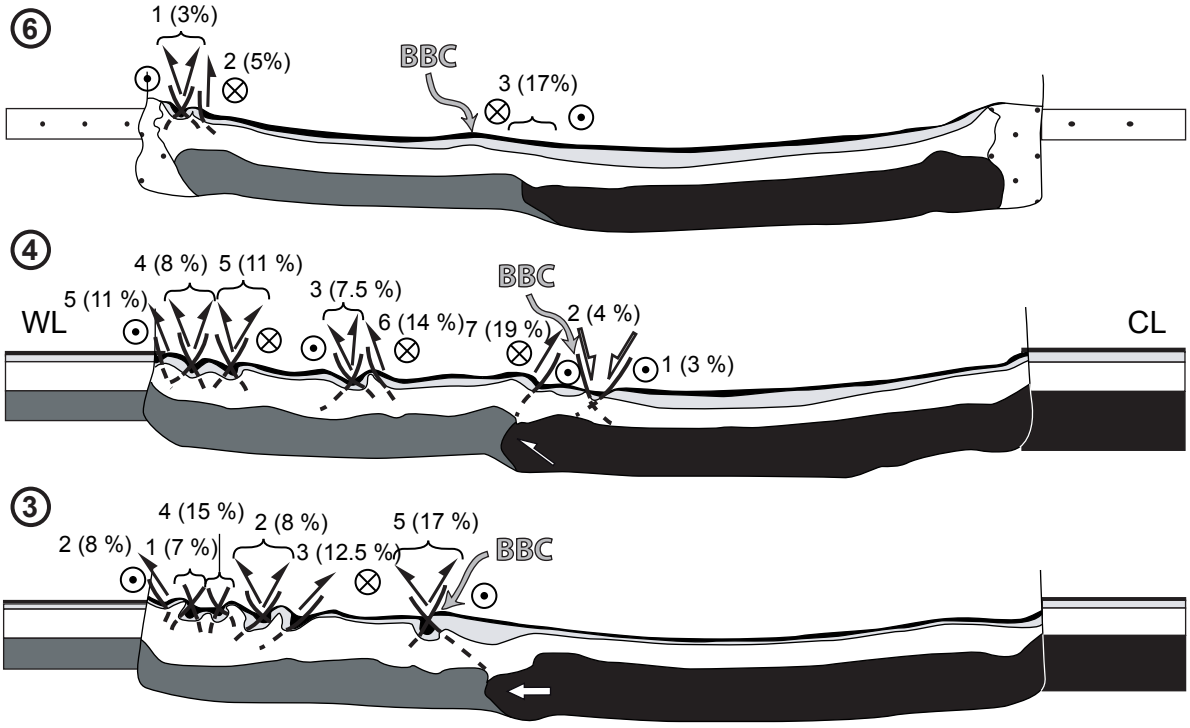

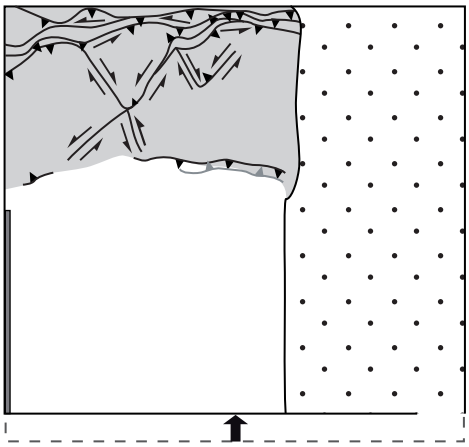

7 % shortening

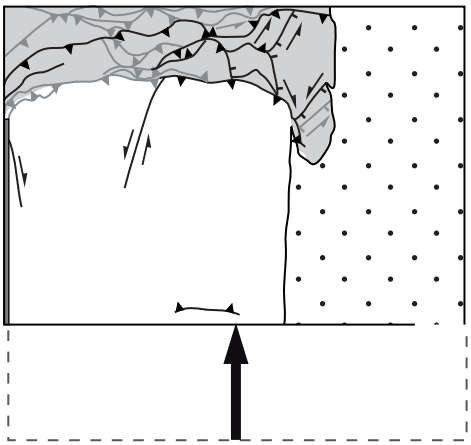

27 %

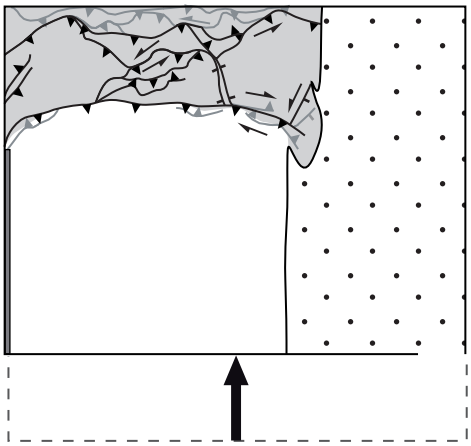

20 %

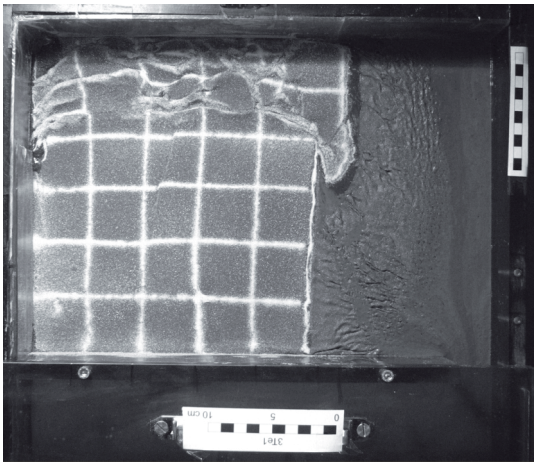

27 %

10 cm

F1 settings:

- free lateral boundary
- 3 cm of neutral silicone
- 40% shortening
- 0.75 cm/h

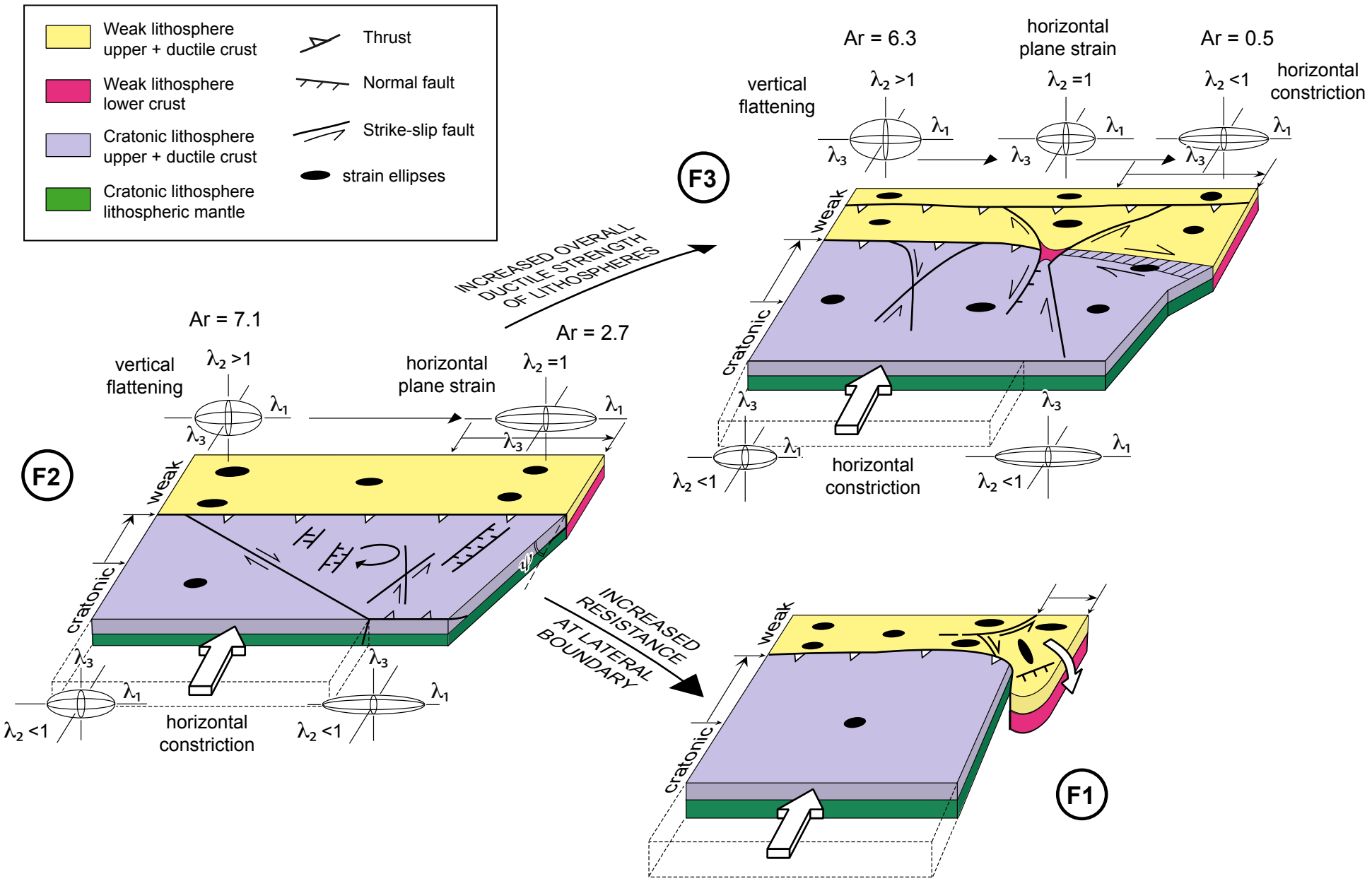
Weak lithosphere upper + ductile crust
Weak lithosphere lower crust
Cratonic lithosphere upper + ductile crust
Cratonic lithosphere lithospheric mantle
Thrust
Normal fault
Strike-slip fault
strain ellipses
F3
Ar = 6.3
horizontal plane strain
Ar = 0.5
vertical flattening
horizontal constriction
INCREASED OVERALL DUCTILE STRENGTH OF LITHOSPHERES
Ar = 7.1
Ar = 2.7
F2
weak
cratonic
INCREASED RESISTANCE AT LATERAL BOUNDARY
F1

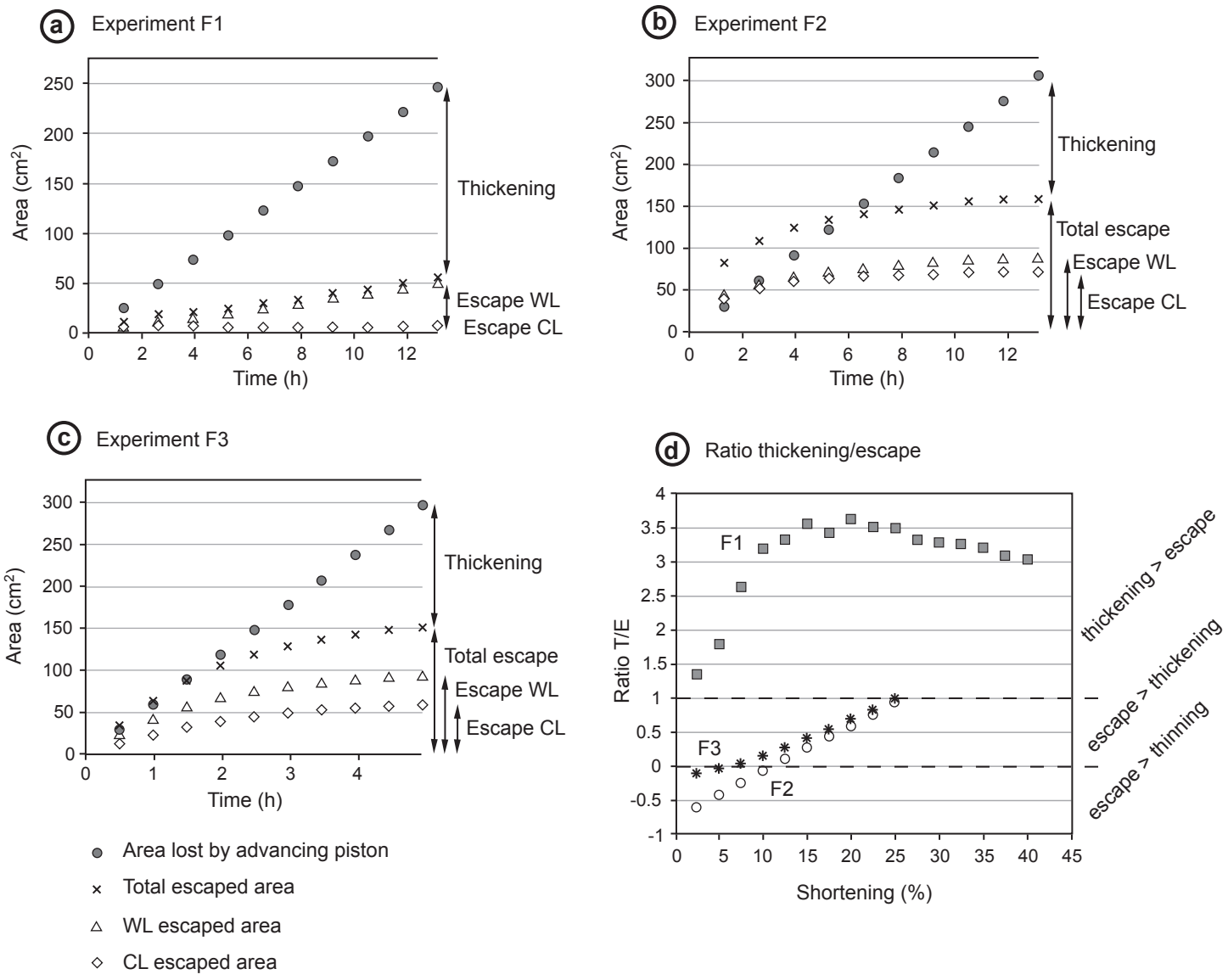
a
Experiment F1
Area (cm²)
Time (h)
Thickening
Escape WL
Escape CL
b
Experiment F2
Area (cm²)
Time (h)
Thickening
Total escape
Escape WL
Escape CL
c
Experiment F3
Area (cm²)
Time (h)
Thickening
Total escape
Escape WL
Escape CL
Area lost by advancing piston
Total escaped area
WL escaped area
CL escaped area
d
Ratio thickening/escape
Ratio T/E
Shortening (%)
F1
F2
F3
thickening > escape
escape > thickening
escape > thinning

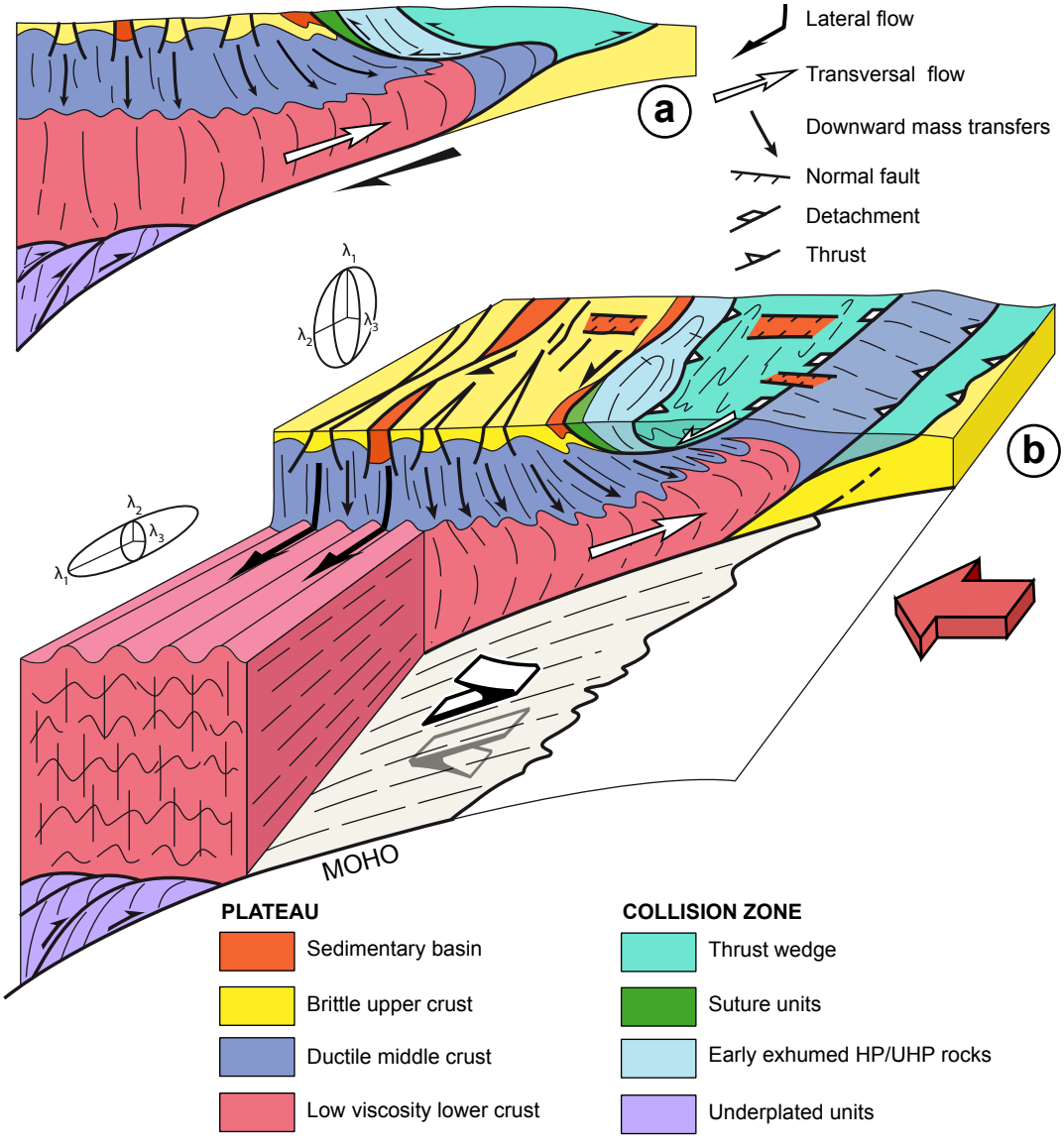
a
b
Lateral flow
Transversal flow
Downward mass transfers
Normal fault
Detachment
Thrust
λ1
λ2
λ3
MOHO
PLATEAU
Sedimentary basin
Brittle upper crust
Ductile middle crust
Low viscosity lower crust
COLLISION ZONE
Thrust wedge
Suture units
Early exhumed HP/UHP rocks
Underplated units

Table 1.

Experiment	Finite shortening (%)	Shortening velocity (cm h^{-1})	Lithosphere size (cm)		Sand thickness (cm)		Used silicones* and thicknesses (cm)
			WL	CL	WL	CL	
Confined boundary							
C1	30	2	27x18	27x21.5	0.5	0.5	DC: 1 WLC: 1 CLM: 2
C2	30	0.75	27x21.5	27x18	0.5	0.5	DC: 1 WLC: 1 CLM: 2
C3	50	0.75	27x21.5	27x18	0.4	0.8	DC: 1 WLC: 1 CLM: 2
C4	50	2	27x20	27x19.5	0.4	0.8	DC: 1 WLC: 1 CLM: 2
C5	50	4	27x19.5	27x20	0.4	0.8	DC: 1 WLC: 1 CLM: 2
C6	50	0.4	27x19.5	27x20	0.4	0.8	DC: WLC: 1 CLM: 2
C7	40	2	27x20	27x19.5	0.4	0.8	DC: 1, + markers TWLC: 2 CLM: 2
C8	40	0.75	27x19.5	27x20	0.4	0.8	DC: 1 TWLC: 2 CLM: 2
Lateral escape							
F1	40	0.75	25x19.5	25x20	0.4	0.8	DC: 0.85 WLC: 1.25 CLM: 2 CS: 3
F2	25	0.75	30.5x19	30.5x20.5	0.4	0.8	DC: 0.8 WLC: 1.2 CLM: 2.1 CS: 1
F3	25	2	30.5x19	30.5x20.5	0.4	0.8	DC: 1 WLC: 1 CLM: 2 CS: 1

* The properties of each silicone are listed in Table 2. CL – cratonic lithosphere; WL – weak lithosphere; DC – ductile crust; WLC – weak lower crust; TWLC – thickened weak lower crust; CLM – cratonic lithospheric mantle; CS – confining silicone.

Table 2.

Materials	Viscosity (Pa s)	Density	Thickness (cm)
Sand + ethyle cellulose	-	1.37	0.4 or 0.8
Sodium polythungstate + glycol water	1.2	1.75	7
Silicones			
Ductile crust (DC) blue	3.57×10^4	1.40	1
Weak lower crust (WLC) purple	2.77×10^4	1.42	1
Thickened weak lower crust (TWLC) brown	9.51×10^3	1.42	2
Cratonic lithospheric mantle (CLM) pink	3.58×10^4	1.56	2
Confining silicone (CS)	5.8×10^3	1.48	1 or 3

Table 3.

Layer	σ_1- σ_3 (Pa)*	
	Shortening rate of 2 cm h^{-1}	Shortening rate of 0.75 cm h^{-1}
Weak lithosphere		
Ductile crust	4.97	1.86
Lower crust	3.90	1.46
Cratonic lithosphere		
Ductile crust	4.97	1.86
Cratonic lithospheric mantle	5.36	2.00

*Strength profiles for a shortening rate of 2 cm h^{-1} are shown in Figure 2.

Table 4.

Experiment	ε_s		Ar initial		Ar final			
					Internal domain		External domain	
	Weak lithosphere	Cratonic lithosphere	Weak lithosphere	Cratonic lithosphere	Weak lithosphere	Cratonic lithosphere	Weak lithosphere	Cratonic lithosphere
F1			-3.2	1.0				
F2	1.4	1.1	8.3	4.0	7.1	1.8	2.7	0.5
F3	1.1	0.9	7.2	3.8	6.3	1.5	0.5	0.6